A&A 581, A60 (2015)
DOI: 10.1051/0004-6361/201526705

Astronomy & Astrophysics

New observations and models of circumstellar CO line emission of AGB stars in the *Herschel* SUCCESS programme⋆,⋆⋆,⋆⋆⋆

T. Danilovich[1], D. Teyssier[2], K. Justtanont[1], H. Olofsson[1], L. Cerrigone[3], V. Bujarrabal[4], J. Alcolea[5], J. Cernicharo[6], A. Castro-Carrizo[7], P. García-Lario[2], and A. Marston[2]

[1] Onsala Space Observatory, Department of Earth and Space Sciences, Chalmers University of Technology, 439 92 Onsala, Sweden
e-mail: taissa@chalmers.se
[2] European Space Astronomy Centre, Urb. Villafranca del Castillo, PO Box 50727, 28080 Madrid, Spain
[3] ASTRON, the Netherlands Institute for Radioastronomy, PO Box 2, 7990 AA Dwingeloo, The Netherlands
[4] Observatorio Astronómico Nacional (IGN), PO Box 112, 28803 Alcalá de Henares, Spain
[5] Observatorio Astronómico Nacional (IGN), Alfonso XII, 3 y 5, 28014 Madrid, Spain
[6] Group of Molecular Astrophysics. ICMM. CSIC. C/ Sor Juana Inés de La Cruz N3, 28049 Madrid, Spain
[7] Institut de Radioastronomie Millimétrique, 300 rue de la Piscine, 38406 Saint-Martin d'Hères, France

Received 9 June 2015 / Accepted 28 June 2015

ABSTRACT

Context. Asymptotic giant branch (AGB) stars are in one of the latest evolutionary stages of low to intermediate-mass stars. Their vigorous mass loss has a significant effect on the stellar evolution, and is a significant source of heavy elements and dust grains for the interstellar medium. The mass-loss rate can be well traced by carbon monoxide (CO) line emission.
Aims. We present new *Herschel*/HIFI and IRAM 30 m telescope CO line data for a sample of 53 galactic AGB stars. The lines cover a fairly large range of excitation energy from the $J = 1 \rightarrow 0$ line to the $J = 9 \rightarrow 8$ line, and even the $J = 14 \rightarrow 13$ line in a few cases. We perform radiative transfer modelling for 38 of these sources to estimate their mass-loss rates.
Methods. We used a radiative transfer code based on the Monte Carlo method to model the CO line emission. We assume spherically symmetric circumstellar envelopes that are formed by a constant mass-loss rate through a smoothly accelerating wind.
Results. We find models that are consistent across a broad range of CO lines for most of the stars in our sample, i.e., a large number of the circumstellar envelopes can be described with a constant mass-loss rate. We also find that an accelerating wind is required to fit, in particular, the higher-J lines and that a velocity law will have a significant effect on the model line intensities. The results cover a wide range of mass-loss rates ($\sim 10^{-8}$ to 2×10^{-5} $M_{\odot}$ yr^{-1}) and gas expansion velocities (2 to 21.5 km s^{-1}) , and include M-, S-, and C-type AGB stars. Our results generally agree with those of earlier studies, although we tend to find slightly lower mass-loss rates by about 40%, on average. We also present "bonus" lines detected during our CO observations.

Key words. stars: AGB and post-AGB – circumstellar matter – stars: evolution – stars: mass-loss

1. Introduction

Towards the end of their lives, low and intermediate mass stars (with masses ~0.8–8 $M_{\odot}$) will exhaust their supply of He and cease fusion reactions in their cores, leaving a quiescent C/O core with H and He fusion reactions only taking place in thin shells surrounding the core. This evolutionary phase is known as the asymptotic giant branch (AGB; Herwig 2005).

AGB stars are also a significant source of heavy elements in the Universe. It is thought that about half of all elements heavier than Fe originate in AGB stars through the *s*-process of slow neutron capture (Herwig 2005). It is during the AGB phase that this enriched material is brought to the surface. At the same time, the star experiences vigorous mass loss, ejecting matter to form a circumstellar envelope (CSE) around the star. Molecules and dust grains form in the CSE, and will eventually chemically enrich the interstellar medium (ISM).

It is believed that AGB stars begin their lives on the AGB as oxygen-rich M-type stars, and eventually some of these, those with masses in the range ~1.5–4 $M_{\odot}$ (Herwig 2005), will transition into carbon-rich C stars. With a C/O ratio close to 1, S stars are believed to occupy the evolutionary phase between M and C stars. The lowest mass AGB stars ($\lesssim 1$ $M_{\odot}$) do not transform into C stars because they do not undergo a third dredge-up event. The highest mass AGB stars ($\gtrsim 4$ $M_{\odot}$) also do not end their lives as C stars due to hot bottom burning (HBB), unless the mass loss quenches the HBB process, leaving time for the star to evolve into a C star before leaving the AGB.

Radiative transfer modelling of circumstellar CO radio lines has long been used to derive the mass-loss rates of AGB stars (Morris 1987; Kastner 1992; Justtanont et al. 1994; Groenewegen 1998; Schöier & Olofsson 2001; Olofsson et al. 2002; Decin et al. 2006; Ramstedt et al. 2009; De Beck et al. 2010). These data were almost exclusively obtained with ground-based telescopes. The *Herschel* Space Observatory

⋆ *Herschel* is an ESA space observatory with science instruments provided by European-led Principal Investigator consortia and with important participation from NASA.
⋆⋆ Based on observations carried out with the IRAM 30 m Telescope. IRAM is supported by INSU/CNRS (France), MPG (Germany) and IGN (Spain).
⋆⋆⋆ Appendices are available in electronic form at http://www.aanda.org

allowed observations of higher energy lines than possible from ground-based telescopes. This has led to studies that model molecular emission (not only that of CO) in more detail and over a wide range of energies as in Schöier et al. (2011), Khouri et al. (2014), and Danilovich et al. (2014). However, each of those papers deals with only one or a handful of stars. The new data have not yet been applied to mass-loss rate determinations for larger samples of stars.

In this paper we present new data obtained as part of the SUbmilimetre Catalogue of Circumstellar EnvelopeS with *Herschel*/HIFI project (SUCCESS, Teyssier et al. 2011), a CO survey of a large sample of AGB and post-AGB stars across all three chemical types. *Herschel*/HIFI was used to observe the CO $J = 5 \rightarrow 4$ and $J = 9 \rightarrow 8$ lines in 53 AGB stars. Of these, six stars were also observed in the CO $J = 14 \rightarrow 13$ line and 29 stars were also observed in the CO $J = 1 \rightarrow 0$ and $J = 2 \rightarrow 1$ lines using the IRAM 30 m telescope. Of these stars we present radiative transfer models for 38 objects, supplementing our new high-resolution observations with archival data where possible. Inclusion of the high-J lines from *Herschel*/HIFI allows us to better constrain our models over a broad range of temperatures, and hence produce models that better represent the CSE over a large radial range.

2. Sample and observations

SUCCESS is a *Herschel*/HIFI Guaranteed Time project (Teyssier et al. 2011) which observed 74 AGB and post-AGB stars in the CO $J = 5 \rightarrow 4$ and $J = 9 \rightarrow 8$ lines, and 10 of those objects also in the CO $J = 14 \rightarrow 13$ line. Excluding post-AGB objects and extreme OH/IR stars (the latter presented in Justtanont et al. 2013), the sample comprised of 53 AGB stars observed in the former two lines and six observed in all three lines. The sample was primarily built based on the evolved star lists considered in the studies by Knapp et al. (1998), Schöier & Olofsson (2001), and Castro-Carrizo et al. (2010), complemented by some of the brightest line calibrators regularly used at the APEX telescope (Güsten et al. 2008). The selection criterion was related to the intensity of the CO $J = 2 \rightarrow 1$ as observed at the IRAM 30 m telescope, and aimed at sources exhibiting peak intensities in excess of 1.5 K ($T_{\rm mb}$) in this line.

A reduced sample of 29 objects was also observed with the IRAM 30 m telescope in the CO $J = 1 \rightarrow 0$ and $J = 2 \rightarrow 1$ lines. The objective was to obtain well-calibrated data observed with state-of-the-art receivers, especially for those sources where the literature spectra dated from several decades ago and/or had been obtained from a varied set of facilities.

The full sample is summarised in Table 1, including the pulsation periods and the systemic velocities. A summary of all our new observations and integrated line intensities is given in Table 2. We have indicated with an * those lines which have some ISM contamination that was corrected for when calculating the integrated intensity. In these cases, the contamination tended to occur only on one side of the line and we calculated the intensity by integrating from the centre to the edge of the non-contaminated side and then doubling this result. The beam-widths for each line and telescope are given in Table 3.

The new data for stars we have modelled are shown in Figs. A.1–A.3. The new observations for stars we have not modelled are shown in Figs. B.1–B.3.

2.1. IRAM observations

The complementary observations at the IRAM 30 m telescope were obtained in December 2013 respectively using the E090 and E230 EMIR receivers and the FTS backend to cover the CO $J = 1 \rightarrow 0$ and $J = 2 \rightarrow 1$ lines. We used the Wobbler Switching mode with a throw of 4′. Owing to the large instantaneous bandwidth offered by the EMIR receivers, several bonus lines from ^{13}CO, CN, SiS, and HC_3N were simultaneously observed and are presented in Sect. 2.4. Data were processed with the GILDAS/Class[1] software and converted into the $T_{\rm mb}$ scale assuming main beam efficiencies of 0.78 and 0.58 at 3 and 1 mm respectively. We have corrected for the antenna elevation gain, which accounts for up to 25% line intensity loss in our data. Finally, we re-adjusted our line intensities based on the monitoring of reference spectra of the CO lines in IRC+10216 (with fiducial line peak intensities of 24.3 K and 54.5 K for the CO $J = 1 \rightarrow 0$ and $J = 2 \rightarrow 1$ lines, respectively), resulting in corrections between 0 and 20% depending on the line and the observing day. The achieved noise root mean square (rms) are in the range 30–150 mK and 55–360 mK at 3 and 1 mm, respectively, and per native velocity resolution element (0.5 and 0.25 km s^{-1}, respectively).

2.2. HIFI observations

The SUCCESS sample was observed between July 2010 and April 2012 using the HIFI instrument (de Graauw et al. 2010) aboard the *Herschel* Space Observatory (Pilbratt et al. 2010). The data were obtained with the double beam switching mode, using reference positions separated by 3′ from the target position (Roelfsema et al. 2012). The spectra were sampled on the Wide Band Acousto-Optical Spectrometer (WBS), offering a native resolution of 1.1 MHz (0.6 km s^{-1} at the lowest observed frequency). The selected frequency tunings were optimised for the targeted CO lines, but bonus lines of CN and SiO were also obtained in the instantaneous bandwidth of 4 GHz (2.4 GHz for the CO $J = 14 \rightarrow 13$ line) provided by the WBS (see Sect. 2.4). The full list of *Herschel* observation identifiers (ObsIDs) is given in Table B.1.

The HIFI data have been processed using HIPE 12[2] and calibrated in the $T_{\rm A}^*$ scale. On top of that, the CO $J = 14 \rightarrow 13$ data have been corrected for the so-called electrical standing waves using the *doHebCorrection* task (Kester et al. 2014). A sideband gain ratio different from unity has been used for the CO $J = 5 \rightarrow 4$ observations (Higgins et al. 2014). Finally, all our data have been converted to the $T_{\rm mb}$ using the revised main beam efficiencies (Müeller et al. 2014[3]). Likewise, we refer to this technical note for the beam size assumed in our modelling (Table 3). The achieved 1σ noise rms was 15 mK ($T_{\rm mb}$) for a smoothed resolution channel of 3 km s^{-1} for both CO $J = 5 \rightarrow 4$ and $J = 9 \rightarrow 8$, and 44 mK for CO $J = 14 \rightarrow 13$.

2.3. Supplementary data

To better constrain our models, we used previously observed low- and intermediate-J CO lines from a variety of sources.

[1] http://www.iram.fr/IRAMFR/GILDAS

[2] HIPE is a joint development by the *Herschel* Science Ground Segment Consortium, consisting of ESA, the NASA *Herschel* Science Center, and the HIFI, PACS, and SPIRE consortia.

[3] http://herschel.esac.esa.int/twiki/pub/Public/HifiCalibrationWeb/HifiBeamReleaseNote_Sep2014.pdf

Table 1. Basic stellar parameters for the AGB stars in the SUCCESS sample.

Star	Alternate name	RA (J2000)	Dec (J2000)	Variability	Period [days]	$\upsilon_{\rm lsr}$ [km s^{-1}]
C stars						
R Scl	IRC−30015	01 26 58.09	−32 32 35.5	SRb	370	−19
V701 Cas	AFGL 482	03 23 36.57	+70 27 07.5	M	567	−14
V384 Per	IRC+50096	03 26 29.53	+47 31 50.2	M	535	−16
GY Cam	IRC+60144	04 35 17.54	+62 16 23.8	SR	...	−47
R Lep	IRC−10080	04 59 36.35	−14 48 22.5	M	445	11
V1259 Ori	AFGL 865	06 03 59.84	+07 25 54.4	M	696	42
IRAS 06192+4657		06 22 58.52	+46 55 34.9	?	...	−23
UU Aur	IRC +40158	06 36 32.84	+38 26 43.8	SRb	235	8
V688 Mon	AFGL 971	06 36 54.24	+03 25 28.7	M	653	3
AI Vol	IRAS 07454 −7112	07 45 02.80	−71 19 43.2	M	511	−39
U Hya	IRC−10242	10 37 33.27	−13 23 04.4	SRb	183	−32
X TrA	IRAS 15094 −6953	15 14 19.18	−70 04 46.1	SR	361	−2
II Lup	IRAS 15194 −5115	15 23 04.91	−51 25 59.0	M	575	−15.5
V CrB	IRC+40273	15 49 31.31	+39 34 17.9	M	358	−99
V821 Her	IRC+20370	18 41 54.39	+17 41 08.5	M	524	−0.5
V Aql	IRC−10486	19 04 24.16	−05 41 05.4	SRb	407	54
V1968 Cyg	AFGL 2494	20 01 08.51	+40 55 40.2	M	783	28
RV Aqr	IRC+00499	21 05 51.68	−00 12 40.3	M	453	1
TX Psc	IRC+00532	23 46 23.52	+03 29 12.5	LB	...	13
S stars						
R And	IRC+40009	00 24 01.95	+38 34 37.3	M	409	−16
S Cas	IRC+70024	01 19 41.97	+72 36 39.3	M	612	−30
W And	IRC+40037	02 17 32.96	+44 18 17.8	M	397	−35
R Gem	IRC+20171	07 07 21.27	+22 42 12.7	M	370	−60
Y Lyn	IRC+50180	07 28 11.61	+45 59 26.2	SRc	110	−0.5
RS Cnc	IRC+30209	09 10 38.80	+30 57 47.3	SRb	242	6.5
R Cyg	IRC+50301	19 36 49.38	+50 11 59.5	M	426	−17
π Gru	AFGL 4289	22 22 44.21	-45 56 52.6	SRb	196	−12
M stars						
KU And	IRC+40004	00 06 52.94	+43 05 00.0	M	720	−22
V370 And	IRC+50049	01 58 44.33	+45 26 06.9	SRb	228	−2
AFGL 292	IRC+10025	02 02 38.63	+07 40 36.5	?	...	23
R Hor	IRAS 02522 −5005	02 53 52.77	−49 53 22.7	M	408	37
NV Aur	IRC+50137	05 11 19.44	+52 52 33.2	M	635	2
BX Cam	IRC+70066	05 46 44.10	+69 58 25.2	M	...	−2
GX Mon	IRC+10143	06 52 46.91	+08 25 19.0	M	527	−9
L_2 Pup	IRAS 07120 −4433	07 13 32.32	−44 38 23.1	SRb	141	33.5
S CMi	IRC+10167	07 32 43.07	+08 19 05.2	M	333	51
R LMi	IRC+30215	09 45 34.28	+34 30 42.8	M	372	0
R Leo	IRC+10215	09 47 33.49	+11 25 43.7	M	310	0
R Crt	IRC−20222	11 00 33.85	−18 19 29.6	SRb	160	11
BK Vir	IRC+00220	12 30 21.01	+04 24 59.2	SRb	140	17
Y UMa	IRC+60220	12 40 21.28	+55 50 47.6	SRb	168	19
RT Vir	IRC+10262	13 02 37.98	+05 11 08.4	SRb	158	18
SW Vir	IRC+00230	13 14 04.39	−02 48 25.2	SRb	146	−11
R Hya	IRC−20254	13 29 42.78	−23 16 52.8	M	380	−10
RX Boo	IRC+30257	14 24 11.63	+25 42 13.4	SRb	158	2
S CrB	IRC+30272	15 21 23.96	+31 22 02.6	M	360	0
X Her	IRC+50248	16 02 39.17	+47 14 25.3	SRb	102	−73
V1111 Oph	IRC+10365	18 37 19.26	+10 25 42.2	M	...	−32
RR Aql	IRC+00458	19 57 36.06	−01 53 11.3	M	395	28
V1943 Sgr	IRC−30425	20 06 55.24	−27 13 29.8	SRb	330	−15
V1300 Aql	IRC−10529	20 10 27.87	−06 16 13.6	M	680	−18
T Cep	IRC+70168	21 09 31.78	+68 29 27.2	M	388	−2
EP Aqr	IRC+00509	21 46 31.85	−02 12 45.9	SRb	55	−34

Notes. An ellipsis (...) indicates an unknown property. Variability and period information was obtained from the International Variable Star Index (VSX) database.

A summary of the supplementary observations is given in Table C.1.

The telescopes and their corresponding beam widths for different frequencies are listed in Table 3, covering all the new and archival observations used in this paper.

As well as archival line data, we have used results from the APEX Pointing Catalogue, which can be found online[4].

[4] http://www.apex-telescope.org/observing/pointing/spectra/

Table 2. HIFI and IRAM CO line observations.

Star	v_∞	IRAM		HIFI		
		CO (1 → 0)	CO (2 → 1)	CO (5 → 4)	CO (9 → 8)	CO (14 → 13)
	[km s^{-1}]	[K km s^{-1}]	[K km s^{-1}]	[K km s^{-1}]	[K km s^{-1}]	[K km s^{-1}]
C stars						
R Scl	16.5	81.9 (1.0)	103.3 (0.9)	5.30 (0.08)	1.57 (0.07)	1.33 (0.38)
V701 Cas	11.5	*36.4 (0.3)	*44.4 (0.4)	1.67 (0.22)	1.93 (0.07)	...
V384 Per	15	63.6 (0.2)	90.1 (0.3)	5.52 (0.18)	6.25 (0.09)	...
GY Cam	20	43.8 (0.2)	70.1 (0.3)	3.14 (0.20)	2.90 (0.08)	...
R Lep	18	32.5 (0.4)	100.3 (0.6)	4.23 (0.13)	4.57 (0.08)	...
V1259 Ori	16	63.8 (0.2)	85.7 (0.3)	3.93 (0.21)	3.23 (0.07)	...
IRAS 06192+4657	6	...	...	<0.22 (0.16)	0.290 (0.171)	...
UU Aur	12	...	...	2.47 (0.15)	2.31 (0.08)	...
V688 Mon	13.5	*30.8 (0.3)	*67.4 (0.2)	1.96 (0.19)	2.31 (0.09)	...
AI Vol	12	...	...	6.87 (0.13)	8.12 (0.08)	7.62 (0.23)
U Hya	6.5	8.87 (0.37)	53.7 (1.0)	2.98 (0.16)	2.07 (0.11)	...
X TrA	6.5	...	...	1.36 (0.18)	1.76 (0.08)	...
II Lup	21.5	...	...	16.8 (0.1)	17.6 (0.07)	...
V CrB	7.5	...	...	0.541 (0.159)	1.07 (0.08)	...
V821 Her	13.5	82.8 (0.5)	136.5 (0.7)	6.32 (0.15)	7.46 (0.08)	...
V Aql	11	12.6 (0.2)	23.1 (0.3)	1.36 (0.13)	1.30 (0.07)	...
V1968 Cyg	20	37.2 (0.3)	!	5.58 (0.18)	5.79 (0.07)	...
RV Aqr	15	46.0 (0.2)	73.9 (0.4)	3.64 (0.13)	4.16 (0.07)	...
TX Psc	4	...	...	0.887 (0.141)	1.24 (0.08)	...
S stars						
R And	8	27.0 (0.4)	56.9 (0.4)	3.72 (0.16)	5.58 (0.08)	...
S Cas	19	37.6 (0.3)	90.9 (0.5)	4.27 (0.18)	6.08 (0.08)	...
W And	6	8.14 (0.1)	24.5 (0.4)	1.07 (0.13)	1.34 (0.09)	...
R Gem	5	7.01 (0.3)	10.9 (0.6)	0.565 (0.230)	0.471 (0.156)	...
Y Lyn	8	11.1 (0.4)	29.6 (0.6)	1.52 (0.19)	1.28 (0.09)	...
RS Cnc	2.5	22.9 (0.2)	63.4 (0.5)	3.60 (0.19)	3.17 (0.08)	...
R Cyg	9	15.6 (0.3)	43.2 (0.5)	2.21 (0.16)	1.42 (0.08)	...
π Gru	10	...	...	13.8 (0.15)	13.9 (0.04)	10.0 (0.1)
M stars						
KU And	20	48.9 (0.3)	83.5 (0.4)	3.15 (0.16)	4.41 (0.07)	...
V370 And	9	...	...	2.96 (0.22)	2.35 (0.09)	...
AFGL 292	8.5	4.56 (0.23)	10.1 (0.2)	0.492 (0.229)	0.481 (0.127)	...
R Hor	4	...	...	4.23 (0.14)	3.31 (0.08)	...
NV Aur	18	43.3 (0.2)	59.1 (0.2)	2.54 (0.13)	1.84 (0.07)	...
BX Cam	19	33.9 (0.2)	50.8 (0.2)	2.96 (0.19)	2.58 (0.08)	...
GX Mon	19	64.2 (0.1)	128.1 (0.2)	5.83 (0.18)	4.07 (0.07)	...
L_2 Pup	2	...	...	1.82 (0.14)	2.56 (0.09)	3.41 (0.24)
S CMi	2	0.608 (0.358)	3.84 (0.60)	0.271 (0.108)	0.436 (0.084)	...
R LMi	7.5	...	...	1.51 (0.13)	1.27 (0.08)	...
R Leo	8.5	...	...	5.86 (0.15)	8.35 (0.08)	...
R Crt	12	...	...	3.57 (0.18)	3.26 (0.08)	...
BK Vir	6	3.73 (0.16)	13.1 (0.2)	0.474 (0.101)	1.03 (0.08)	...
Y UMa	7.5	...	...	0.735 (0.088)	0.807 (0.090)	...
RT Vir	8.5	...	...	1.90 (0.14)	1.53 (0.10)	...
SW Vir	8.5	...	...	4.34 (0.23)	4.14 (0.09)	...
R Hya	10	...	...	6.94 (0.22)	7.85 (0.09)	3.98 (0.17)
RX Boo	10	...	...	4.52 (0.23)	3.79 (0.09)	2.92 (0.24)
S CrB	7	3.19 (0.33)	!	1.19 (0.11)	0.910 (0.092)	...
X Her	8.5	...	...	2.37 (0.18)	1.98 (0.08)	...
V1111 Oph	17	47.2 (0.3)	82.1 (0.4)	3.13 (0.19)	2.50 (0.07)	...
RR Aql	9	...	...	1.50 (0.11)	1.14 (0.08)	...
V1943 Sgr	6.5	...	...	0.862 (0.168)	0.754 (0.082)	...
V1300 Aql	18	68.9 (0.4)	102.7 (0.7)	3.66 (0.15)	3.12 (0.06)	...
T Cep	5.5	...	...	1.44 (0.10)	1.90 (0.09)	...
EP Aqr	12	...	...	3.73 (0.16)	3.35 (0.08)	...

Notes. The value in brackets after the flux gives the integrated noise rms. An ellipsis (...) indicates that the line was not observed for the indicated star; (*) indicates that flux has been corrected for ISM emission; (!) indicates the line was observed but with unreliable flux calibration.

For our spectral energy distribution (SED) models we primarily used photometry from IRAS and 2MASS (Høg et al. 2000). See Sect. 3.1 for more details.

2.4. Bonus lines

In the course of our new HIFI and IRAM observations, we also acquired some "bonus" line spectra for molecules that were

Table 3. Telescope parameters for all lines referred to in this paper.

Transition	Frequency [GHz]	Telescope	θ [″]
CO (1 → 0)	115.271	IRAM	21.4
		NRAO	55
		OSO	33
		SEST	45
CO (2 → 1)	230.538	APEX	27
		CSO	30
		IRAM	10.7
		JCMT	21
		SEST	23
CO (3 → 2)	345.796	APEX	18
		CSO	20
		JCMT	14
		SEST	15
CO (4 → 3)	461.041	APEX	14
		CSO	15.5
		JCMT	12
CO (5 → 4)	576.268	HIFI	36.1
CO (6 → 5)	691.473	CSO	10.3
		HIFI	30.4
		JCMT	8
CO (7 → 6)	806.652	APEX	7.7
CO (9 → 8)	1036.912	HIFI	20.1
CO (10 → 9)	1151.985	HIFI	18.2
CO (14 → 13)	1611.794	HIFI	12.9
CO (16 → 15)	1841.345	HIFI	11.5

Notes. APEX is the Atacama Pathfinder Experiment; CSO is the Caltech Submillimeter Observatory; IRAM refers to the 30 m telescope at the Institut de Radioastronomie Millimétrique; JCMT is the *James Clerk Maxwell* Telescope; HIFI is the Heterodyne Instrument for the Far-Infrared aboard *Herschel*; NRAO refers to the 12 m telescope at the (US) National Radio Astronomy Observatory; OSO is the 20 m telescope at the Onsala Space Observatory; SEST is the Swedish-ESO submillimetre telescope.

observable within our target frequency ranges. Our HIFI observations covered the CN ($5_{9/2} \rightarrow 4_{7/2}$) and ($5_{11/2} \rightarrow 4_{9/2}$) line groups, which were detected in a handful of C stars, and SiO (13 → 12), which was detected mostly in M stars. Our IRAM observations covered the CN $N = 1 \rightarrow 0$ and CN $N = 2 \rightarrow 1$ line groups, which were detected in most C stars and one S star (S Cas). Also covered by IRAM were the ^{13}CO (1 → 0) line, which was detected in most observed sources, the SiS (6 → 5) line, which was detected in higher mass-loss rate sources, and the HC_3N (12 → 11) line, which was detected in the higher mass-loss rate C stars.

We will not be modelling these additional species but we discuss the bonus detections in greater detail in Sect. B.2. The observations are plotted in Figs B.4–B.7. The integrated intensities for the detected lines are listed in Table B.2.

3. Radiative transfer modelling

3.1. SED modelling

We begin our radiative transfer modelling by estimating some key dust properties of each star in the sample. The SED modelling is performed using DUSTY[5], a publicly available radiative transfer code (Ivezic & Elitzur 1997). We found the best fit for each star using primarily 2MASS and IRAS photometric observations. The distances taken from the literature and the luminosities were calculated from the period-luminosity relation of Glass & Evans (1981):

$$M_{\rm bol} = 0.76 - 2.09 \log P. \quad (1)$$

The resulting effective temperature of the central black body, dust optical depth (given at 10 μm) and the inner radius of our model, based on the dust condensation temperature, are listed in Table 4.

As the DUSTY code has been widely used, some of the stars in our sample have already been modelled using the same methods and in these cases we simply use the earlier results from Schöier et al. (2007, 2013), and Ramstedt & Olofsson (2014). These are indicated with a † in Table 4.

3.2. CO line modelling

3.2.1. The circumstellar model

In our radiative transfer modelling of the observed CO lines, we assumed a spherically symmetric CSE, formed through constant and isotropic mass loss with a smoothly accelerating wind. Some of our modelled stars, such as GY Cam and AFGL 292, show line profiles which we are not able to reproduce within our adopted circumstellar model. See Sect. 4.4 for further discussion of this.

The radial gas velocity law used in our modelling is given by

$$\upsilon(r) = \upsilon_{\rm min} + (\upsilon_\infty - \upsilon_{\rm min})\left(1 - \frac{R_{\rm in}}{r}\right)^\beta \quad (2)$$

where $\upsilon_{\rm min} = 3$ km s^{-1} is the approximate sound speed at the dust condensation radius, υ_∞ is the observed terminal expansion velocity, $R_{\rm in}$ is the dust condensation radius as calculated in the corresponding SED model, and β is a parameter used to adjust the acceleration in the inner part of the envelope. In general, we assume $\beta = 1.0$ but adjust it for the stars where this gives a noticeable improvement in the fits to the line shapes. The β values used for each star are given in Table 5. For some stars we use a constant expansion velocity, either because the line width is especially low (such as for S CMi and L_2 Pup with $\upsilon_\infty = 2$ km s^{-1}) or because the constant velocity model was a much better fit to the observations than a model with a velocity profile. The range of results is discussed in more detail in Sect. 4.4. We also employ a constant turbulent gas velocity of 0.5 km s^{-1} for all the modelled stars.

A similar function to Eq. (2) is used for the dust and drift velocities, where the drift velocity is the difference between the dust and gas velocities. The terminal drift velocity is assumed to be (for details see Kwok 1975):

$$\upsilon_{\rm drift,\infty} = \sqrt{\frac{L_* \upsilon_\infty Q}{\dot{M} c}} \quad (3)$$

where L_* is the stellar luminosity, $\dot{M}$ is the mass-loss rate, Q is an efficiency factor assumed to be 0.03 (Ramstedt et al. 2008), and c is the speed of light. The drift velocity profile is calculated from Eq. (2) with this terminal velocity and with $\upsilon_{\rm min} = 1$. For each star, the same $R_{\rm in}$ and β values are used for the drift (and hence dust) velocity as for the corresponding gas velocity. Where the gas velocity has $\beta_{\rm gas} = 0$, we assume that the drift velocity has $\beta_{\rm drift} = 1$. Using this formulation, we find drift velocities in the range 2–18 km s^{-1} (with a median of 6 km s^{-1}), which is below the sputtering-dominated threshold of 20 km s^{-1} calculated by Kwok (1975).

[5] http://www.pa.uky.edu/~moshe/dusty/

Table 4. SED parameters.

Star	D [pc]	L_* [$L_\odot$]	T_* [K]	τ_{10}	R_{in} [$\times 10^{14}$ cm]	Reference
C stars						
V701 Cas	1720	7800	2800	0.85	2.1	Menzies et al. (2006)
V384 Per	560	8100	2000	0.25	2.1	† Schöier et al. (2013)
GY Cam	1030	7800	2000	0.3	2.0	Groenewegen et al. (2002)
R Lep	432	5500	2200	0.06	1.7	† Ramstedt & Olofsson (2014)
V1259 Ori	1600	9300	2200	1.7	2.2	Menzies et al. (2006)
UU Aur	260	6900	2800	0.017	1.9	† Schöier et al. (2013)
V688 Mon	1770	8800	2800	0.6	2.2	Menzies et al. (2006)
AI Vol	710	9000	2100	0.45	2.2	† Schöier et al. (2007)
U Hya	208	*4000	2400	0.012	1.5	† Ramstedt & Olofsson (2014)
X TrA	360	5400	2200	0.024	1.7	Cox et al. (2012)
II Lup	500	8800	2400	0.55	2.2	† Schöier et al. (2013)
V CrB	630	5300	1800	0.035	1.7	Cox et al. (2012)
V821 Her	600	7900	2200	0.45	2.1	† Schöier et al. (2013)
V Aql	330	6500	2800	0.02	1.9	† Schöier et al. (2013)
V1968 Cyg	1480	10200	2400	0.85	2.3	Menzies et al. (2006)
RV Aqr	670	6800	2200	0.27	1.9	† Schöier et al. (2013)
S stars						
R And	350	6300	1900	0.05	1.8	† Ramstedt & Olofsson (2014)
S Cas	570	8000	1800	0.5	2.1	† Ramstedt & Olofsson (2014)
W And	450	5800	2400	0.1	1.8	van Leeuwen (2007)
R Gem	820	5500	2400	0.035	1.7	Whitelock et al. (2008) ‡
Y Lyn	253	*4000	2400	0.02	1.5	Ramstedt & Olofsson (2014)
R Cyg	690	6200	2600	0.14	1.8	Whitelock et al. (2008) ‡
M stars						
KU And	680	11800	2000	0.90	2.5	† Schöier et al. (2013)
AFGL 292	319	*6000	2200	0.02	1.8	Winters et al. (2003)
R Hor	310	8500	2200	0.30	2.1	† Schöier et al. (2013)
NV Aur	1200	9800	2000	3.50	2.3	† Schöier et al. (2013)
BX Cam	500	7500	2800	1.30	2.0	† Schöier et al. (2013)
GX Mon	550	8200	2600	2.00	2.1	† Schöier et al. (2013)
L_2 Pup	86	*4000	2800	0.07	1.5	Schöier et al. (2013)
S CMi	470	5000	2800	0.07	1.6	Knapp et al. (1998)
R LMi	330	5500	2400	0.2	1.7	Whitelock et al. (2008) ‡
R Leo	130	4600	1800	0.10	1.6	† Schöier et al. (2013)
S CrB	400	5400	2400	0.2	1.7	Knapp et al. (1998)
V1111 Oph	750	7500	2000	0.75	2.0	† Schöier et al. (2013)
RR Aql	530	7900	2000	0.70	2.1	† Schöier et al. (2013)
V1943 Sgr	200	5000	2200	0.05	1.6	van Leeuwen (2007)
V1300 Aql	620	10600	2000	3.50	2.4	† Schöier et al. (2013)
T Cep	190	5700	2400	0.10	1.8	van Leeuwen (2007)

Notes. An * indicates that the luminosity is assumed (for semi-regular variables) rather than calculated. The references listed are for distances, D, and in some cases the luminosity, L, where no period is known. A † in the references indicates that all parameters including the effective temperature, T_*, and optical depth, τ_{10} were also taken from the referenced DUSTY modelling. The absence of a † indicates that temperature and optical depth were calculated as part of this work. ‡ indicates that the distance was calculated from the period-magnitude relation in the cited work.

3.2.2. The modelling approach

We modelled the observed CO lines using a Monte Carlo program (MCP) which has been previously described in Bernes (1979), Schöier & Olofsson (2001), Schöier et al. (2002), Ramstedt et al. (2008), and Danilovich et al. (2014). The MCP code takes basic stellar and molecular parameters, and the results of our SED model as input and calculates the molecular excitation by solving the statistical equilibrium equations using the Monte Carlo method. MCP also solves the energy balance equation to calculate the gas temperature as a function of radius throughout the CSE,

$$\frac{\mathrm{d}T_{\rm kin}}{\mathrm{d}r} = (2-2\gamma)\left(1+\frac{r}{2\upsilon(r)}\frac{\mathrm{d}\upsilon}{\mathrm{d}r}\right)\frac{T_{\rm kin}(r)}{r} + \frac{\gamma-1}{n_{\rm H_2}k_{\rm B}\upsilon(r)}(H-C) \quad (4)$$

where $T_{\rm kin}$ is the kinetic temperature of the gas, $n_{\rm H_2}$ is the hydrogen number density, $k_{\rm B}$ is Boltzmann's constant, γ is the adiabatic index with $\gamma = \frac{5}{3}$ for $T_{\rm kin} < 350$ K and $\gamma = \frac{7}{5}$ otherwise, and H and C are the sums of the heating and cooling terms, respectively. The adiabatic cooling is given by the first term on the right-hand side of the equation. Otherwise, the cooling terms include H_2 vibrational line cooling and CO rotational line cooling, and the heating terms include heating due to dust-gas collisions and photoelectric heating. CO line cooling can also act as heating in some circumstances (for more details, see Schöier & Olofsson 2001).

The most important heating term in the energy balance equation, the dust-gas collision term, includes a number of assumptions on the dust properties. These come in a multiplicative form and we combine them in the so called h-parameter defined as

$$h = \left(\frac{\Psi}{0.01}\right)\left(\frac{2.0\ \mathrm{g\ cm^{-3}}}{\rho_{\rm d}}\right)\left(\frac{0.05\ \mu\mathrm{m}}{a_{\rm g}}\right) \quad (5)$$

Table 5. CSE parameters from CO models.

Star	$\dot{M}$ [$M_\odot$ yr^{-1}]	β	h	$\chi^2_{\rm red}$	N
C stars					
V701 Cas	4.5×10^{-6}	0	5×10^{0}	5.1	4
V384 Per	2.3×10^{-6}	0	6×10^{-1}	2.8	12
GY Cam	3.7×10^{-6}	2.0	9×10^{-1}	2.0	5
R Lep	8.7×10^{-7}	2.0	5×10^{-2}	1.4	9
V1259 Ori	8.8×10^{-6}	3.0	5×10^{0}	1.7	9
UU Aur	1.7×10^{-7}	1.0	9×10^{-3}	2.3	8
V688 Mon	6.1×10^{-6}	1.0	5×10^{0}	0.58	5
AI Vol	4.9×10^{-6}	1.0	9×10^{-1}	0.76	9
U Hya	8.9×10^{-8}	5.0	8×10^{-2}	2.1	15
X TrA	1.9×10^{-7}	1.0	5×10^{-1}	1.0	9
II Lup	1.7×10^{-5}	0	5×10^{-1}	1.7	20
V CrB	3.3×10^{-7}	1.0	2×10^{-1}	3.2	7
V821 Her	3.0×10^{-6}	1.0	7×10^{-1}	2.7	14
V Aql	1.3×10^{-7}	0	5×10^{-1}	2.0	11
V1968 Cyg	7.5×10^{-6}	1.0	8×10^{0}	2.0	5
RV Aqr	2.3×10^{-6}	1.0	5×10^{-1}	3.4	7
S stars					
R And	5.3×10^{-7}	1.5	6×10^{-1}	1.8	6
S Cas	2.8×10^{-6}	1.0	5×10^{-1}	2.4	6
W And	2.8×10^{-7}	3.0	4×10^{-1}	0.93	5
R Gem	4.3×10^{-7}	2.0	6×10^{-1}	2.2	5
Y Lyn	1.7×10^{-7}	1.5	5×10^{-2}	0.92	5
R Cyg	9.5×10^{-7}	2.0	1×10^{0}	1.9	5
M stars					
KU And	9.4×10^{-6}	2.0	3×10^{-2}	1.7	7
AFGL 292	2.1×10^{-7}	1.0	5×10^{-2}	3.5	4
R Hor	5.9×10^{-7}	1.0	4×10^{-1}	0.19	6
NV Aur	2.5×10^{-5}	1.0	6×10^{-1}	1.8	11
BX Cam	4.4×10^{-6}	1.0	5×10^{-3}	3.1	7
GX Mon	8.4×10^{-6}	1.0	5×10^{-1}	2.6	14
L_2 Pup	1.4×10^{-8}	0	2×10^{-1}	1.3	10
S CMi	4.9×10^{-8}	0	6×10^{-1}	1.2	4
R LMi	2.6×10^{-7}	2.0	2×10^{-1}	2.2	6
R Leo	1.1×10^{-7}	5.0	5×10^{-2}	5.7	15
S CrB	2.3×10^{-7}	5.0	2×10^{-1}	3.9	10
V1111 Oph	1.2×10^{-5}	1.0	6×10^{-1}	1.9	10
RR Aql	2.4×10^{-6}	2.0	5×10^{-2}	2.7	7
V1943 Sgr	9.9×10^{-8}	1.0	5×10^{-3}	3.1	4
V1300 Aql	1.0×10^{-5}	1.0	6×10^{-2}	4.6	16
T Cep	9.1×10^{-8}	1.0	3×10^{-1}	0.23	3

where Ψ is the dust-to-gas ratio, $\rho_{\rm d}$ is the dust grain density and $a_{\rm g}$ is the dust grain radius, assuming spherical grains. We assume $\rho_{\rm d}$ = 2.2 g cm^{-3} for carbon dust and $\rho_{\rm d}$ = 3.3 g cm^{-3} for silicate dust, and $a_{\rm g}$ = 0.05 μm. The h parameter is one of the two free parameters adjusted (in practice we vary Ψ) in our modelling to fit the observational data, the other being the mass-loss rate. The impact of the h-parameter is on the kinetic temperature structure of the CSE, which tends to be close to a power law for part of the envelope. The molecular excitation analysis is complex and therefore the effect of changing h is not always easily predictable, but the tuning of the h parameter finally results in a kinetic temperature distribution that best matches the observed data, in particular the relative intensities of the different J lines. However, since we may be missing terms in the energy balance equation, or the included terms do not fully capture the physics involved, it is clear that the resulting Ψ of the best-fit model is not necessarily a good estimate of the circumstellar dust-to-gas ratio.

Our CO analyses assumed inner CO fractional abundances (with respect to H_2) of 1×10^{-3} for C stars, 6×10^{-4} for S stars and 3×10^{-4} for M stars, in line with canonical results. The sizes of the CO envelopes, which are determined by photodissociation, were calculated using the results of Mamon et al. (1988).

In our CO excitation analyses we included radiative transitions for the first 40 rotational energy levels in the ground and first vibrationally excited states, taken from Chandra et al. (1996). The collisional rates, which were only available for the ground vibrational state, were taken from Yang et al. (2010) and weighted assuming an ortho-/para-H_2 ratio of 3 by Schöier et al. (2011). They cover kinetic temperatures from 2 to 3000 K.

We calculated the best fit models for each star using a χ^2 statistic, which we define as

$$\chi^2 = \sum_{i=1}^{N} \frac{(I_{{\rm mod},i} - I_{{\rm obs},i})^2}{\sigma_i^2} \quad (6)$$

where I is the integrated line intensity, σ is the uncertainty in the observations (generally assumed to be 20%), and N is the number of lines being modelled. We also calculate a reduced χ^2 value such that $\chi^2_{\rm red} = \chi^2/(N-p)$ where p is the number of free parameters. We take the mass-loss rate and the h parameter as the two free parameters, i.e. p = 2. (Although β is also adjusted, it is done so based solely on the line widths and not the complete model results.)

In Fig. 1 we show the resultant molecular emission line models plotted against observational data for two C stars: U Hya, which is a low mass-loss rate object, and AI Vol, which is a higher mass-loss rate object. Alongside our model results for U Hya (shown in blue) we have plotted the results of the same model with the only alteration being a constant velocity instead of a velocity law following Eq. (2) (red dashed line). As can be clearly seen, the constant velocity model severely under-predicts the higher-J lines, compared with both the observations and the standard model with a velocity profile. This is a good example of both the importance of considering high-J lines when constraining a model, and the effect of using a velocity profile. Figure 2 shows model and observations for Y Lyn, a low mass-loss rate S star, and S Cas, a higher mass-loss rate S star. Figure 3 shows model and observations for L_2 Pup, a very low mass-loss rate (and low expansion velocity) M star, and KU And, a higher mass-loss rate M star.

The remainder of our results are plotted in Figures A.1–A.3 and the model results are summarised in Table 5. We plot new HIFI and IRAM observations where they are available, and archival ($1\rightarrow0$) and ($2\rightarrow1$) lines where new low-J observations are missing, to show as broad a range of lines with respect to J as possible.

4. Analysis and discussion

4.1. Modelling target selection

Not all the stars in our observational sample were modelled in this paper. Some stars, such as the semi-regular variables (SRV) BK Vir, RX Boo, R Crt, Y UMa, SW Vir, RT Vir, X Her, and EP Aqr, will be modelled in a forthcoming paper (Alcolea et al., in prep.), while some were excluded because we knew a priori that our one-dimensional code, in which spherical symmetry is assumed, could not take their idiosyncrasies into account.

The new observations for unmodelled carbon stars can be seen in Fig. B.1. R Scl was excluded because it is known to

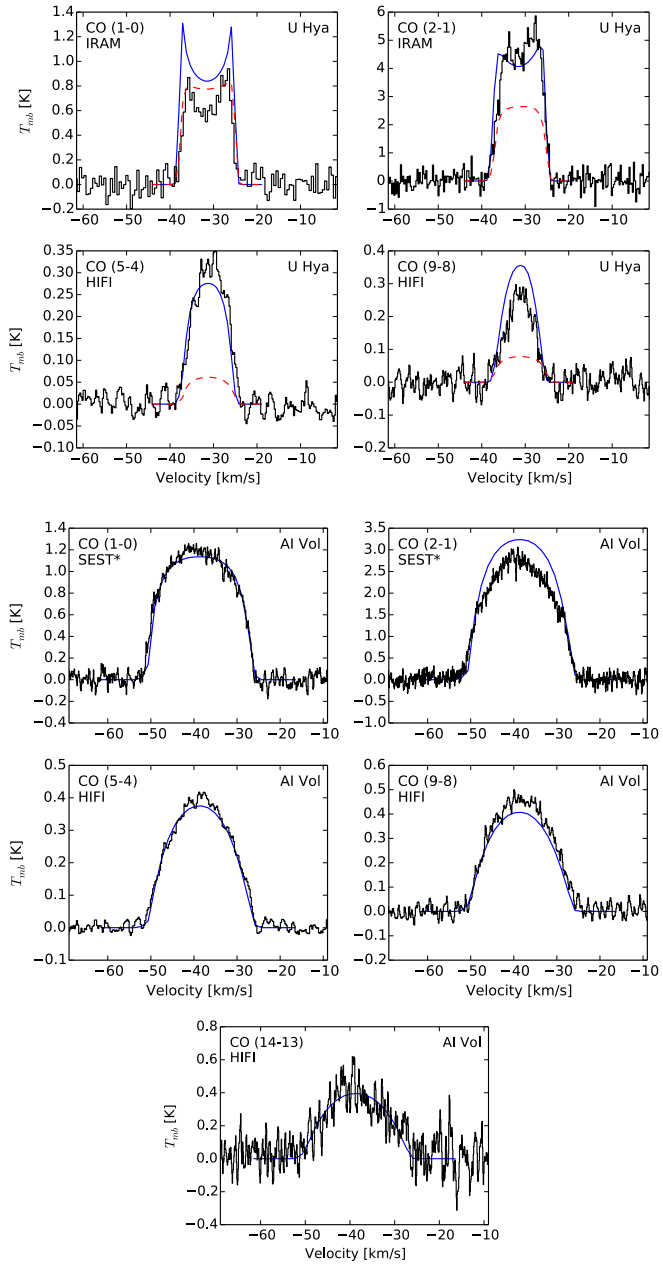

Fig. 1. Models (blue) and observed data (black) of two example C stars, plotted with respect to LSR velocity. An * next to the telescope name indicates that archival data is plotted. The dashed red lines on U Hya show the predicted model if a constant expansion velocity is used, keeping all parameters the same as in the blue model.

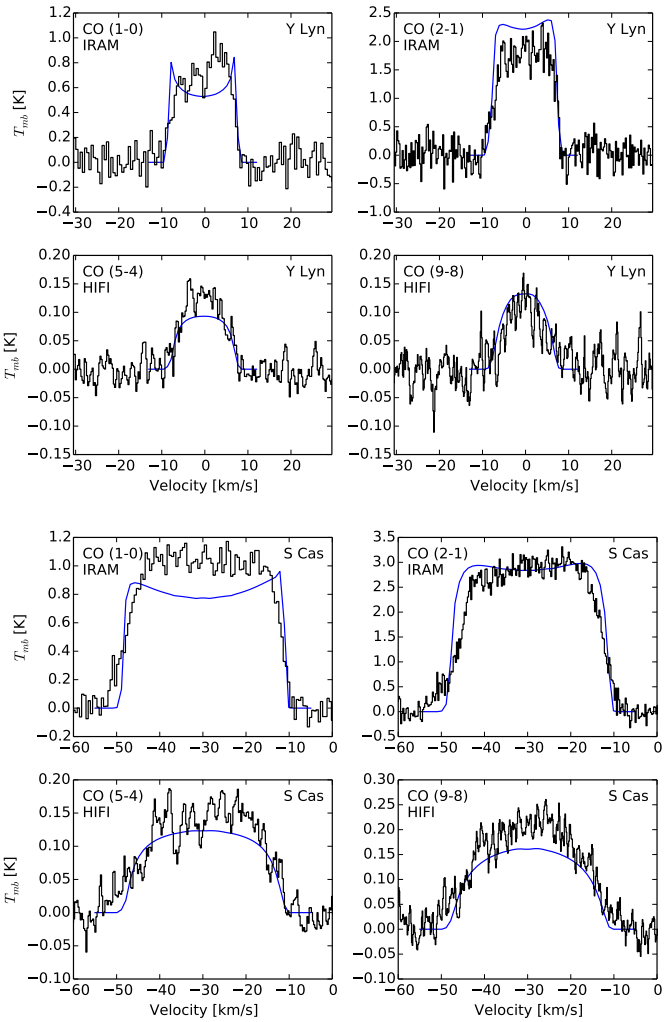

Fig. 2. Models (blue) and observed data (black) of two example S stars, plotted with respect to LSR velocity.

have a detached shell and a spiral structure in the gas indicative of an unseen companion (Maercker et al. 2012). See also Schöier et al. (2005) for a discussion of difficulties modelling this particular star. Conversely, U Hya is also known to have a detached shell (Waters et al. 1994), but the shell is sufficiently distant that the CO in it is most likely photodissociated and hence it has no impact on the detected CO lines, enabling us to keep U Hya in our modelled sample. IRAS 06192+4657 was excluded because we had insufficient data for a robust model, particularly since the (5 → 4) HIFI line was not convincingly detected. TX Psc was discounted because it has a two-component molecular wind, and is known to have an irregular structure as discussed in Heske et al. (1989).

Two S stars were excluded from modelling, RS Cnc and π^1 Gru, both of which have two velocity components in their line profiles, as can be seen in Fig. B.2. RS Cnc is known to have a bipolar outflow and a disc structure around the star (Libert et al. 2010), and π^1 Gru is known to have a bipolar outflow, a G0V binary companion, and evidence of a second hidden companion, as described by Mayer et al. (2014).

The unmodelled M-type star sample contains the SRVs listed above and R Hya and V370 And, which were excluded for having double component winds.

These exclusions have left us with a sample for which we have plotted histograms of mass-loss rates and expansion velocities by chemical type in Fig. 4. Note in particular the gap in expansion velocity for M stars with no modelled stars in the range 10 km s^{-1} ≤ υ_∞ < 15 km s^{-1}. There is a similar gap in the S star distribution, however this is more a result of having only one S star of high mass-loss rate and high velocity. The C stars are fairly evenly distributed in velocity.

4.2. Goodness of fit

The goodness of fit of our models has been primarily estimated using the χ^2 method discussed in Sect. 3.2. To further visualise the goodness of fit we have plotted the values of modelled line

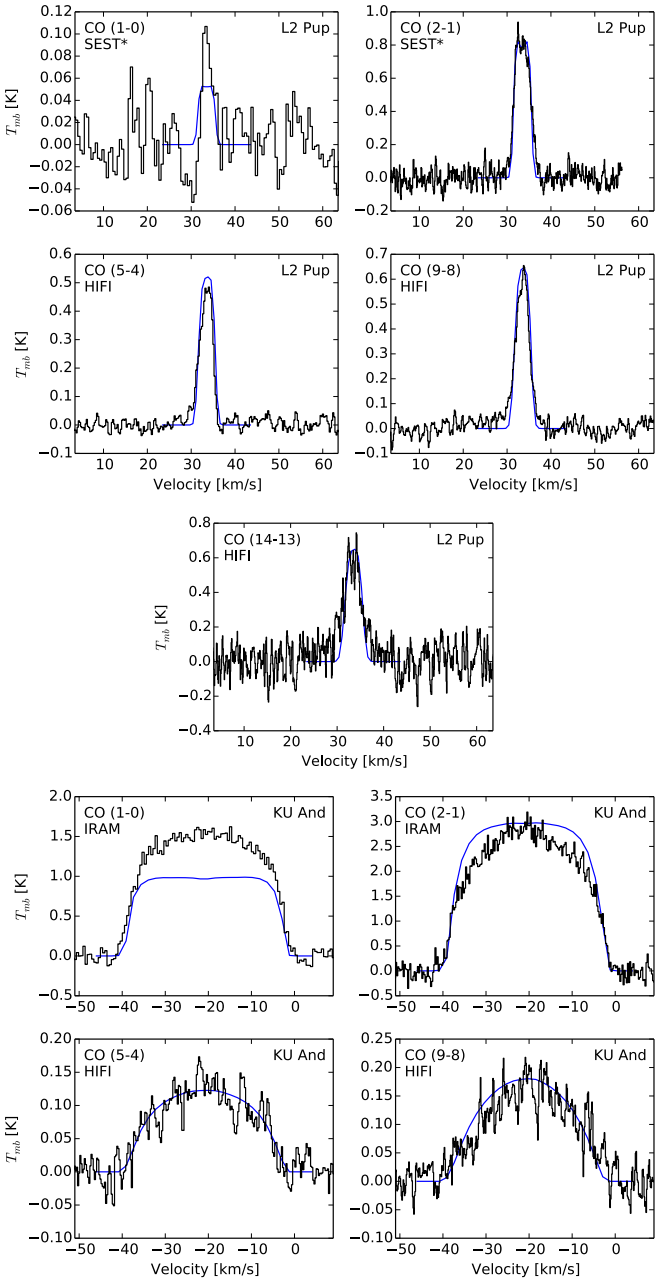

Fig. 3. Models (blue) and observed data (black) of two example M stars, plotted with respect to LSR velocity. An * next to the telescope name indicates that archival data is plotted.

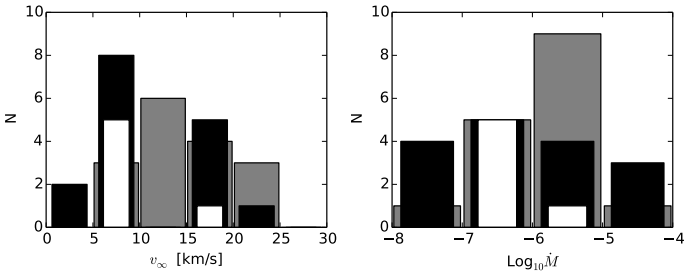

Fig. 4. The numbers of stars with the indicated expansion velocities and mass-loss rates. C stars are grey, S stars are white and M stars are black.

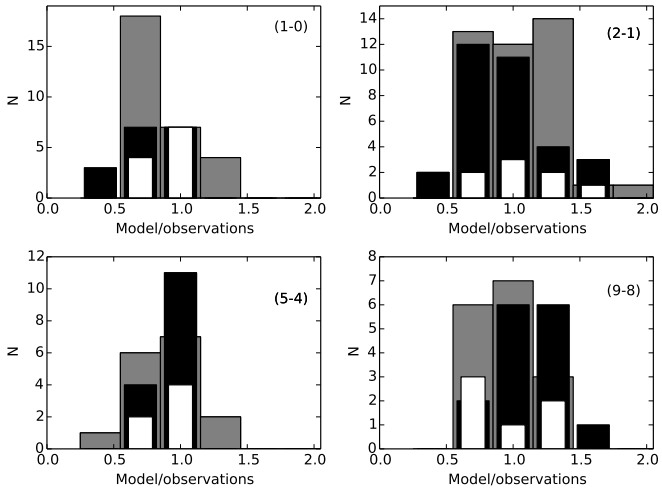

Fig. 5. Goodness of fit as defined by model/observed integrated line intensity of all stars per transition line for C (grey), S (white) and M (black) stars. N is the number of lines of each chemical type in each bin.

intensity divided by the observed line intensity ($I_{\rm mod}/I_{\rm obs}$) for each observed line in each star. The resulting plots can be seen in Fig. A.4 for C stars, Fig. A.5 for S stars and Fig. A.6 for M stars. For the large majority of sources, we can model the CO lines with upper energy levels below 250 K (and below 580 K for sources with observed $J = 14 \rightarrow 13$ lines) with reasonably accuracy using a constant mass-loss rate. In particular, there is no trend with J-number.

We have also combined the same quantity for all stars grouped by line, for the $(1 \rightarrow 0)$, $(2 \rightarrow 1)$, $(5 \rightarrow 4)$, and $(9 \rightarrow 8)$ lines. The resultant plots can be seen in Fig. 5. The distributions are reasonably symmetric, except for the $(1 \rightarrow 0)$ that seems to be under-predicted in the models for all three chemical types. The $(1 \rightarrow 0)$ line intensity is particularly sensitive to the size of the CO envelope and the former discrepancy can be (at least partly) remedied if a larger CO envelope is used than the size predicted by the Mamon et al. (1988) model.

However, this line, and to some extent the $(2 \rightarrow 1)$ line also have a tendency to towards double-peaked profiles rather than the flat or slightly rounded observed line profiles. This happens in about 5 out of 38 cases and is a well-known fact in CO line modelling, for example see Olofsson et al. (2002). An increase in the size of the CO envelope would further enhance the double-peaked nature of the line profiles. In addition to the CO envelope size, there are several possible reasons for the double-peaked $(1 \rightarrow 0)$ line profiles: a too-warm outer CSE, a too-distant source, or maser action in the inner CSE (which was in evidence in some of our models but is known to be produced in nature). Since we have studied a large sample of sources in this paper, we have preferred to treat all sources the same and, therefore, make no adjustments for individual sources. consequently, we conclude that we produce overall good fits to the CO line intensities for the majority of our sources. while there remain some discrepancies (some known from previous studies, such as the tendency for double-peaked model line profiles), we believe they have no major impact on the conclusions in this paper.

4.3. Trends with mass-loss rate and chemical type

To investigate any trends that appear in our results, we plotted mass-loss rate against luminosity, expansion velocity, optical depth at 10 μm, and the h parameter in Fig. 6. There is a clear

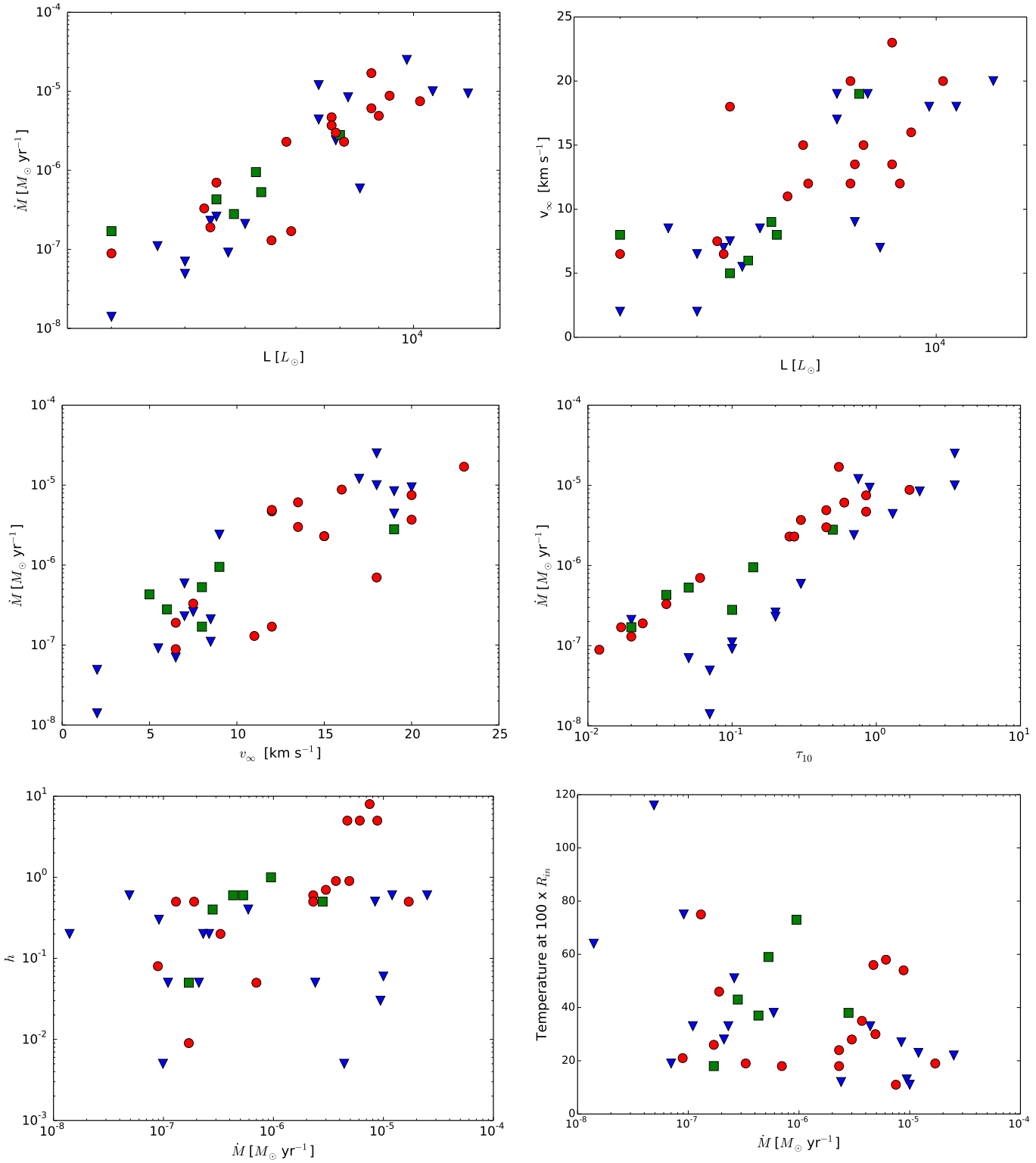

Fig. 6. Mass-loss rate and expansion velocity plotted against luminosity; mass-loss rate plotted against expansion velocity, optical depth and the h-parameter; temperature in the CSE at a radius of $100 \times R_{\rm in}$ plotted against mass-loss rate. Carbon stars are red circles, S stars are green squares, M stars are blue triangles.

trend between mass-loss rate and luminosity, which does not seem to depend on chemical type. This is in line with the expectation that the higher luminosity stars should have higher mass-loss rates, either due to having a higher mass, or due to a more advanced age on the AGB. There is also a correlation between expansion velocity and stellar luminosity, although it is less tight than the mass-loss rate and luminosity correlation. This suggests that the gas expansion velocity is tied to the stellar luminosity. It is not surprising, then to find a correlation between the mass-loss rate and gas expansion velocity. The relation between these two

mass-loss characteristics puts constraints on any viable mass-loss mechanism. Although there is some segregation in both of these plots, this is due to gaps in our sample rather than intrinsic trends.

There is also a correlation between mass-loss rate and optical depth at 10 μm, as is expected if the gas and dust mass-loss rates are correlated. The correlation has slightly different slopes for the C and M stars. For C stars we find the best fit slope is 1.0 ± 0.3 and for M stars 1.3 ± 0.6. There are not enough S stars in our sample for a meaningful determination. It should also be noted that the optical depth is taken at 10 μm, near a strong silicate feature in the M stars and an SiC feature in the C stars. This probably contributes to the difference in slope, along with differences in wind-driving efficiency between the two chemical types.

The plot of mass-loss rate against h parameter does not show any obvious trends, indicating that the dust properties embedded in the h parameter do not directly depend on the mass-loss rate.

We have modelled CO lines covering a relatively broad range in energies, which means that the kinetic temperature distribution is well constrained, except perhaps for the very inner part. In Fig. 6 (bottom right) we plot the kinetic temperature in the CSE at a radius of $100 \times R_{\rm in}$ against mass-loss rate. There is no obvious correlation, but the trend is that the CSEs become, on average, cooler the higher the mass-loss rate. This is certainly expected, since, with all else being equal, a high mass-loss rate leads to more efficient CO line cooling and a lower drift velocity contributing to less efficient heating of the gas.

4.4. Comments on individual stars

For the discussion of individual stars below, note that the modelled and observed lines plotted in Figs. 1–3, and in Figs A.1–A.3, show a maximum of five emission lines. In most cases there are several archival observations which were included in the modelling, and are listed in Table C.1, but are not plotted with the new observations. These archival observations can have a significant impact on the choice of best fit model. The full collection of line observations for each star is included in the goodness of fit plots in Figs. A.4–A.6. The number of lines included in the radiative transfer modelling for each star is noted in Table 5.

4.4.1. C stars

V1259 Ori, V688 Mon, AI Vol, V821 Her, V1968 Cyg, and RV Aqr all have higher mass-loss rates (above 10^{-6} $M_\odot$ yr^{-1}) and expansion velocities in excess of 10 km s^{-1}. Their CO line profiles can all be described by models that include a velocity profile as described in Eq. (2) with $\beta = 1$, except for in the case of V1259 Ori for which $\beta = 3$. V688 Mon has ISM contamination in the low-J data for which we compensated when calculating the integrated line intensities.

UU Aur, U Hya, X TrA, and V CrB are the low mass-loss rate carbon stars, all having mass-loss rates lower than 10^{-6} $M_\odot$ yr^{-1} and expansion velocities $\leq$10 km s^{-1}. Their CO line profiles are all reasonably well-described by our models with $\beta = 1$, except for in the case of U Hya for which $\beta = 5$. U Hya also has the lowest mass-loss rate (8.9×10^{-8} $M_\odot$ yr^{-1}) of the carbon stars in this sample.

There were a handful of stars for which a constant velocity model ($\beta = 0$) gave a markedly better fit than the standard velocity profile model. The stars which fell into this group were V701 Cas, V384 Per, V Aql, and II Lup. The first two objects have moderate mass-loss rates and V Aql has a relatively low mass-loss rate for a C star. The models of these three objects all suffer from maser emission in the low-J lines if a velocity profile is used (which does not entirely disappear in V Aql even with a constant velocity as can be seen in Fig. A.1). The model maser emission arises in the inner regions of the CSE. It may be that, for various reasons, such maser action is not produced in nature. V701 Cas also suffers from ISM contamination in the low-J lines which was compensated for. II Lup is both a high mass-loss rate and high expansion velocity object. The line intensities of a $\beta > 0$ model do not match the observed data as well as a constant velocity model by a significant amount: the best fit $\beta = 1$ model has $\chi^2_{\rm red} = 3.3$ compared with $\chi^2_{\rm red} = 1.7$ for the constant velocity model.

GY Cam has a narrow component (~8 km s^{-1} wide) lying approximately at the systemic velocity of $\upsilon_{\rm lsr} = -49$ km s^{-1} that is clearly visible in the $(1 \rightarrow 0)$, $(2 \rightarrow 1)$ and $(5 \rightarrow 4)$ lines. Note that it is absent in the $(9 \rightarrow 8)$ line, which suggests that it may be cooler in temperature than the gas contributing to the broader component of the line profile. Our CO model was not able to take the narrow component in these lines into account and we did not compensate for it in any way. Since our best-fit models are determined from total line intensity, this had a slight effect on our result. However, it does not seem to have been as large an issue as in some stars such as AFGL 292 (see Sect. 4.4.3 below).

4.4.2. S stars

The majority of the S stars were straightforward to model. Although R And, R Gem, and Y Lyn are known to have binary companions (Proust et al. 1981; Pourbaix et al. 2003), this did not seem to have any significant impact on the observed line profiles when compared to the line models. The most problematic of these five stars was R Gem, which has the noisiest data.

The only S star which we found problematic to model was S Cas. It has the largest terminal expansion velocity (more than a factor of two higher than any of the other S stars) and we found it to also have the highest mass-loss rate. It was also the only S star for which we detected any CN "bonus" lines (see Sect. B.2). In these ways it bears many similarities to some of the carbon stars.

4.4.3. M stars

KU And, NV Aur, BX Cam, GX Mon, V1111 Oph, and V1300 Aql are the oxygen-rich stars in our sample with the highest terminal expansion velocities ($\upsilon_\infty > 15$ km s^{-1}). They can all be described well by models which include a velocity profile with $\beta = 1$ except for NV Aur, for which $\beta = 2$. It should also be noted that the NV Aur lines exhibit some ISM contamination, especially in the low-J lines.

R Hor, R LMi, S CrB, RR Aql, V1943 Sgr, and T Cep have relatively low terminal expansion velocities, with $\upsilon_\infty <$ 10 km s^{-1}. Their CO profiles are described well by our models and have velocity profiles with β in the range $1.0 \leq \beta \leq 2.0$.

L_2 Pup and S CMi both appear to have very low terminal expansion velocities, with $\upsilon_\infty = 2$ km s^{-1}, and we have therefore modelled the CO line emission in both cases assuming a constant velocity. The fits to the observed lines are in general very good, although it is unclear whether the S CMi $(1 \rightarrow 0)$ line is really as strongly double-peaked as it appears, in which case this behaviour is not reproduced in our model.

However, there are indications that L_2 Pup has a central toroidal or disc structure (Lykou et al. 2015; Kervella et al. 2014), with a possible close companion and bipolar outflow (Kervella et al. 2015). In this case, our spherically symmetric model most likely does not represent a realistic view of L_2 Pups circumstellar environment, and the narrow line is not produced in a slowly, spherically expanding envelope. Similarly, Ragland et al. (2006) have found evidence of asymmetry in S CMi, suggesting non-spherical geometry.

AFGL 292 appears to have a two-component line profile. The new IRAM observations in particular suggest an additional narrow component centred at the stellar systemic velocity. This component is not visible in the high-J lines observed with HIFI, which could be an effect of cooler gas or simply because the signal-to-noise ratio of the HIFI observations is insufficient. As a result, the model we present in Fig. A.3 is the best fit based on the integrated intensities, but does not match the line profiles, particularly not for the low-J lines.

R Leo shows asymmetric line profiles, with the HIFI lines being less bright on the red-shifted side, as can be seen in Fig. A.3. Conversely, some of the low-J lines, most notably the (2 → 1) IRAM line and the (3 → 2) CSO line, have significant peaks on the red side of the line profiles. Also, the (1 → 0) IRAM line seems to have a central peak as well as two outer peaks. This could be indicative of localised clumps of gas at different temperatures.

4.5. Comparison with other studies

We compared our modelling results with those of other studies of stars in our sample. Correcting the mass-loss rates for both different distances to the object and different CO abundance assumptions, we compared results using the metric $\dot{M}_{\rm previous}/\dot{M}_{\rm new}$, where "previous" indicates the mass-loss rate found in an earlier study and "new" refers to our mass-loss rate results. The previous studies with the largest overlap with our sample were those of Schöier & Olofsson (2001), Knapp et al. (1998), De Beck et al. (2012), and Ramstedt & Olofsson (2014). Where possible we also included an extra data point for each star, coming from other overlapping studies such as Olofsson et al. (1993), Woods et al. (2003), Neri et al. (1998), Ramstedt et al. (2008), Teyssier et al. (2006), Young (1995), and Olofsson et al. (2002). Grouping all the comparison ratios into chemical type, we find the mean ratio and standard deviation for C stars is 1.4 ± 0.9, for M stars is 1.4 ± 0.8 and for S stars is 1.9 ± 0.8. The collected ratios are also plotted in histograms in Fig. 7.

In general, our models tend to give mass-loss rates on average 40% lower than previous studies, even after correcting for distances and and CO abundance assumptions. Apart from this offset, the spread in the estimates is about ±50%. We present the first study where high-J lines up to (9 → 8) – or in some cases (14 → 13) – are used in the analysis of a large sample of stars. It could hence be inferred that taking high-J lines properly into account when modelling mass-loss rates results in lower predicted mass-loss rates. Another possible factor is in our use of the velocity profile described in Eq. (2). As discussed in Sect. 3.2.2 and shown in Fig. 1, the inclusion of an accelerating wind model compared with a constant expansion velocity wind can have a significant effect on the resultant line intensities (and intensity ratios between different lines).

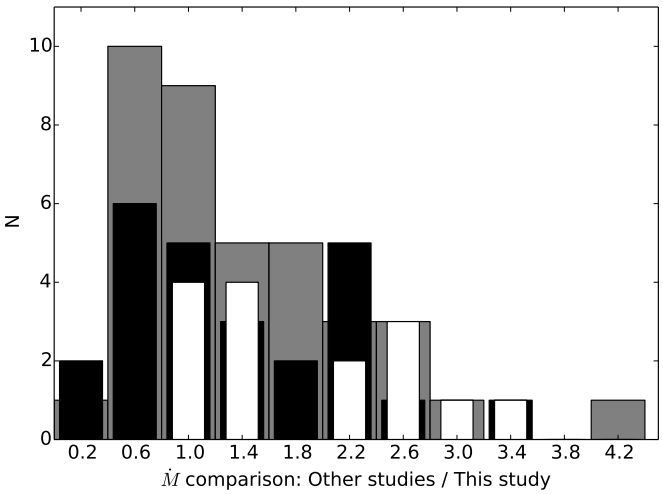

Fig. 7. Comparisons with mass-loss rates from past studies: $\dot{M}_{\rm previous}/\dot{M}_{\rm new}$, grouped by chemical type. C stars are grey, M stars are black and S stars are white.

5. Conclusions

We have presented new *Herschel*/HIFI and IRAM CO line data for a sample of 53 AGB stars, which cover a wide range of transitions from $J = 1 \rightarrow 0$ up to $J = 9 \rightarrow 8$ (and $J = 14 \rightarrow 13$ in a few cases). For 38 of the stars, we used radiative transfer models to determine their mass-loss rates. Our results cover a wide range of mass-loss rates, from $\sim 10^{-8}$–$2 \times 10^{-5} M_\odot$ yr^{-1}, and include all three chemical types of AGB stars (M, S, and C). In general, we find it possible to get a very good fit to the observed CO lines which cover up to 250 K in energy (in a few cases up to 600 K) without the need to invoke mass-loss rate changes with time. Our model results are also in reasonable agreement with past studies (within a factor two for 63% of the stars), although they generally predict slightly lower mass-loss rates than past studies based primarily on lower-J lines. We found that our models under-predict the CO (1 → 0) line intensity more often than other lines, although the precise reason for this is not clear.

In analysing our results we found correlations between mass-loss rate and stellar luminosity, gas terminal expansion velocity, and dust optical depth. The latter correlation seems to show slightly different slopes for the M and C stars, with the S stars falling in between the two. We also found that there is a tendency for the CSEs to have a lower kinetic temperature the higher the mass-loss rate, an effect expected due to less efficient dust-gas collision heating and stronger CO line cooling in the denser objects.

We also found that the inclusion of an expansion velocity profile in our models can have a significant effect on the results. In particular, the use of a constant velocity instead of an accelerating wind can severely under-predict the high-J line intensities, such as those observed by *Herschel*/HIFI. The exact shape of the velocity profile is obtained by fitting the shapes of, in particular, the higher-J lines.

Our observations also included a series of "bonus" lines, which fell within the observing ranges of our CO observations. ^{13}CO was the most commonly detected "bonus" line in all three chemical types of AGB stars. It was detected in eight C stars, five S stars and eight M stars. CN and HC_3N were detected in C stars, with one S star (S Cas) also being detected in some of the observed CN lines. SiO was frequently detected in M stars

(17 detections), as opposed to the C stars where only two were detected. SiS was detected in the higher mass-loss rate C and M stars, although not in all of the highest mass-loss rate stars. There were seven detections in C stars and five in M stars.

Acknowledgements. T.D. and K.J. acknowledge funding from the SNSB. D.T. acknowledges support from the Faculty of the European Space Astronomy Centre (ESAC). HIFI has been designed and built by a consortium of institutes and university departments from across Europe, Canada and the USA under the leadership of SRON Netherlands Institute for Space Research, Groningen, The Netherlands, and with major contributions from Germany, France and the USA. Consortium members are: Canada: CSA, U.Waterloo; France: CESR, LAB, LERMA, IRAM; Germany: KOSMA, MPIfR, MPS; Ireland: NUI Maynooth; Italy: ASI, IFSI-INAF, Osservatorio Astrofisico di Arcetri-INAF; The Netherlands: SRON, TUD; Poland: CAMK, CBK; Spain: Observatorio Astronómico Nacional (IGN), Centro de Astrobiología (CSIC-INTA); Sweden: Chalmers University of Technology – MC2, RSS & GARD; Onsala Space Observatory; Swedish National Space Board, Stockholm University – Stockholm Observatory; Switzerland: ETH Zurich, FHNW; USA: Caltech, JPL, NHSC. This publication is based on data acquired with the Atacama Pathfinder Experiment (APEX). APEX is a collaboration between the Max-Planck-Institut für Radioastronomie, the European Southern Observatory, and the Onsala Space Observatory. This research has made use of the International Variable Star Index (VSX) database, operated at AAVSO, Cambridge, Massachusetts, USA.

References

Bernes, C. 1979, A&A, 73, 67
Castro-Carrizo, A., Quintana-Lacaci, G., Neri, R., et al. 2010, A&A, 523, A59
Chandra, S., Maheshwari, V. U., & Sharma, A. K. 1996, A&AS, 117, 557
Cox, N. L. J., Kerschbaum, F., van Marle, A.-J., et al. 2012, A&A, 537, A35
Danilovich, T., Bergman, P., Justtanont, K., et al. 2014, A&A, 569, A76
De Beck, E., Decin, L., de Koter, A., et al. 2010, A&A, 523, A18
De Beck, E., Lombaert, R., Agúndez, M., et al. 2012, A&A, 539, A108
de Graauw, T., Helmich, F. P., Phillips, T. G., et al. 2010, A&A, 518, L6
Decin, L., Hony, S., de Koter, A., et al. 2006, A&A, 456, 549
Glass, I. S., & Evans, T. L. 1981, Nature, 291, 303
González Delgado, D., Olofsson, H., Kerschbaum, F., et al. 2003, A&A, 411, 123
Groenewegen, M.A.T., & De Jong, T. 1998, A&A, 337, 797
Groenewegen, M. A. T., Sevenster, M., Spoon, H. W. W., & Pérez, I. 2002, A&A, 390, 511
Güsten, R., Baryshev, A., Bell, A., et al. 2008, in SPIE Conf. Ser., 7020, 10
Herwig, F. 2005, ARA&A, 43, 435
Heske, A., te Lintel Hekkert, P., & Maloney, P. R. 1989, A&A, 218, L5
Higgins, R., Teyssier, D., Borys, C., et al. 2014, Exp. Astron., 37, 433
Høg, E., Fabricius, C., Makarov, V. V., et al. 2000, A&A, 355, L27
Ivezic, Z., & Elitzur, M. 1997, MNRAS, 287, 799
Justtanont, K., Skinner, C. J., & Tielens, A. G. G. M. 1994, ApJ, 435, 852
Justtanont, K., Teyssier, D., Barlow, M. J., et al. 2013, A&A, 556, A101
Kastner, J. H. 1992, ApJ, 401, 337
Kemper, F., Stark, R., Justtanont, K., et al. 2003, A&A, 407, 609
Kerschbaum, F., & Olofsson, H. 1999, A&AS, 138, 299
Kerschbaum, F., Olofsson, H., & Hron, J. 1996, A&A, 311, 273
Kervella, P., Montargès, M., Ridgway, S. T., et al. 2014, A&A, 564, A88
Kervella, P., Montargès, M., Lagadec, E., et al. 2015, A&A, 578, A77
Kester, D., Avruch, I., & Teyssier, D. 2014, in Bayesian Inference and Maximum Entropy Methods in Science and Engineering, AIP Conf. Proc. 1636, 62
Khouri, T., de Koter, A., Decin, L., et al. 2014, A&A, 561, A5
Knapp, G. R., Young, K., Lee, E., & Jorissen, A. 1998, ApJS, 117, 209
Kwok, S. 1975, ApJ, 198, 583
Libert, Y., Winters, J. M., Le Bertre, T., Gérard, E., & Matthews, L. D. 2010, A&A, 515, A112
Lykou, F., Klotz, D., Paladini, C., et al. 2015, A&A, 576, A46
Maercker, M., Mohamed, S., Vlemmings, W. H. T., et al. 2012, Nature, 490, 232
Mamon, G. A., Glassgold, A. E., & Huggins, P. J. 1988, ApJ, 328, 797
Mayer, A., Jorissen, A., Paladini, C., et al. 2014, A&A, 570, A113
Menzies, J. W., Feast, M. W., & Whitelock, P. A. 2006, MNRAS, 369, 783
Morris, M. 1987, PASP, 99, 1115
Neri, R., Kahane, C., Lucas, R., Bujarrabal, V., & Loup, C. 1998, A&AS, 130, 1
Olofsson, H., Eriksson, K., Gustafsson, B., & Carlstrom, U. 1993, ApJS, 87, 267
Olofsson, H., Lindqvist, M., Nyman, L.-A., & Winnberg, A. 1998, A&A, 329, 1059
Olofsson, H., González Delgado, D., Kerschbaum, F., & Schöier, F. L. 2002, A&A, 391, 1053
Pilbratt, G. L., Riedinger, J. R., Passvogel, T., et al. 2010, A&A, 518, L1
Pourbaix, D., Platais, I., Detournay, S., et al. 2003, A&A, 399, 1167
Proust, D., Ochsenbein, F., & Pettersen, B. R. 1981, A&AS, 44, 179
Ragland, S., Traub, W. A., Berger, J.-P., et al. 2006, ApJ, 652, 650
Ramstedt, S., & Olofsson, H. 2014, A&A, 566, A145
Ramstedt, S., Schöier, F. L., Olofsson, H., & Lundgren, A. A. 2008, A&A, 487, 645
Ramstedt, S., Schöier, F. L., & Olofsson, H. 2009, A&A, 499, 515
Roelfsema, P. R., Helmich, F. P., Teyssier, D., et al. 2012, A&A, 537, A17
Ryde, N., Schöier, F. L., & Olofsson, H. 1999, A&A, 345, 841
Schöier, F. L., & Olofsson, H. 2001, A&A, 368, 969
Schöier, F. L., Ryde, N., & Olofsson, H. 2002, A&A, 391, 577
Schöier, F. L., Olofsson, H., Wong, T., Lindqvist, M., & Kerschbaum, F. 2004, A&A, 422, 651
Schöier, F. L., Lindqvist, M., & Olofsson, H. 2005, A&A, 436, 633
Schöier, F. L., Olofsson, H., & Lundgren, A. A. 2006, A&A, 454, 247
Schöier, F. L., Bast, J., Olofsson, H., & Lindqvist, M. 2007, A&A, 473, 871
Schöier, F. L., Maercker, M., Justtanont, K., et al. 2011, A&A, 530, A83
Schöier, F. L., Ramstedt, S., Olofsson, H., et al. 2013, A&A, 550, A78
Teyssier, D., Hernandez, R., Bujarrabal, V., Yoshida, H., & Phillips, T. G. 2006, A&A, 450, 167
Teyssier, D., Alcolea, J., Bujarrabal, V., et al. 2011, in The Molecular Universe, eds. J. Cernicharo, & R. Bachiller, IAU Symp., 280, 353
van Leeuwen, F. 2007, A&A, 474, 653
Waters, L. B. F. M., Loup, C., Kester, D. J. M., Bontekoe, T. R., & de Jong, T. 1994, A&A, 281, L1
Whitelock, P. A., Feast, M. W., & van Leeuwen, F. 2008, MNRAS, 386, 313
Winters, J. M., Le Bertre, T., Jeong, K. S., Nyman, L.-Å., & Epchtein, N. 2003, A&A, 409, 715
Woods, P. M., Schöier, F. L., Nyman, L.-Å., & Olofsson, H. 2003, A&A, 402, 617
Yang, B., Stancil, P. C., Balakrishnan, N., & Forrey, R. C. 2010, ApJ, 718, 1062
Young, K. 1995, ApJ, 445, 872

Pages 14 to 33 are available in the electronic edition of the journal at http://www.aanda.org

Appendix A: Modelled stars

Here we present the observations and models for the stars not included in the body of the paper. In each instance, we present all new data from IRAM and HIFI – black histograms – overplotted with model results for the parameters given in Table 5. For those stars that were not observed with IRAM, we include archival CO (1 → 0) and (2 → 1) lines from various telescopes as available. These archival lines are indicated by an * next to the telescope name in the plot and allow us to present an overview of our models from low- to high-J. R Hor is the only star for which these low-J lines were not available. Our model for R Hor still incorporates some low-J lines as noted in Table C.1.

The plots for C stars are shown in Fig. A.1, for S stars in Fig. A.2 and for M stars in Fig. A.3.

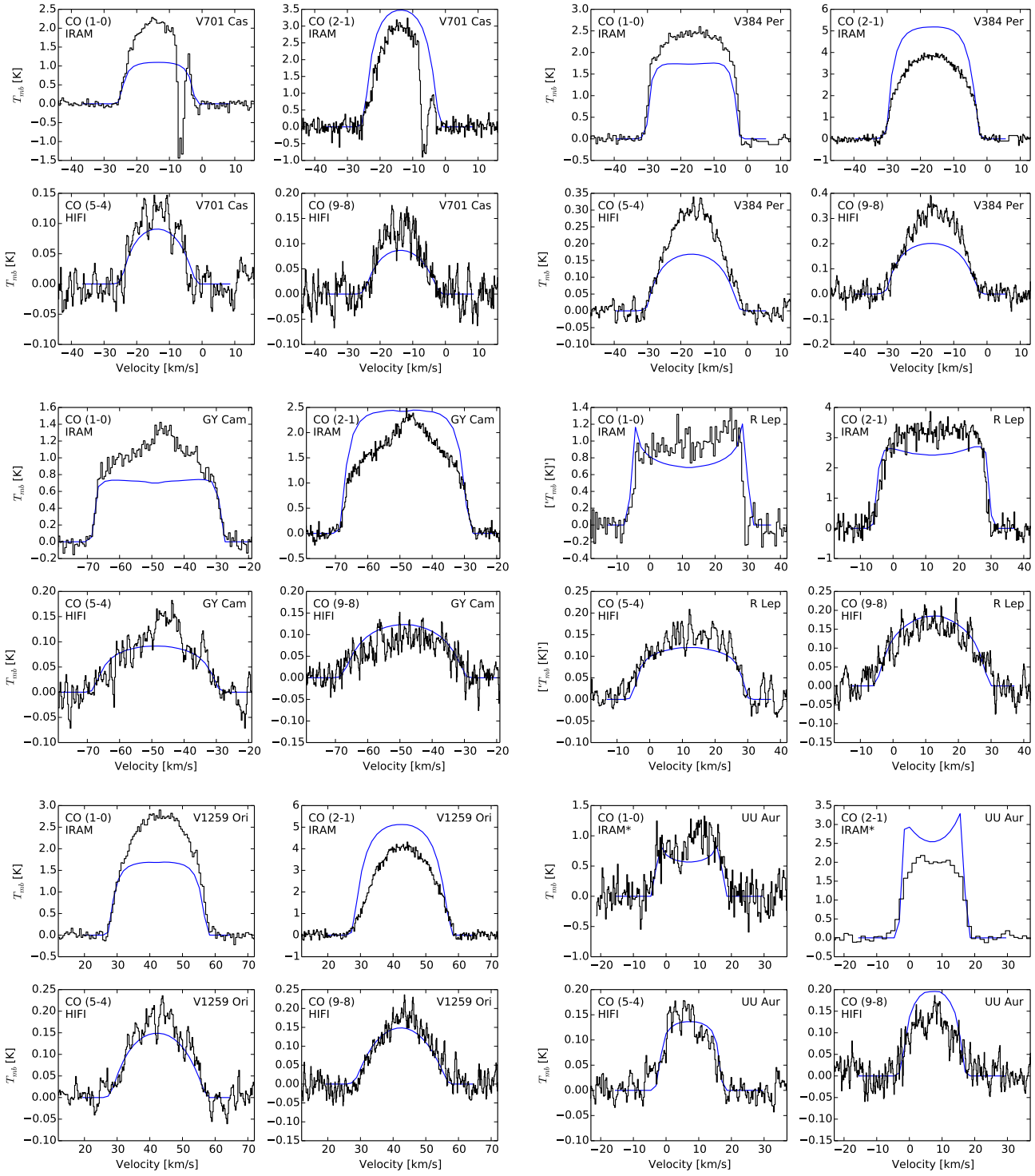

Fig. A.1. Models (blue) and observed data (black) of C stars, plotted with respect to LSR velocity. An * next to the telescope name indicates that archival data is plotted.

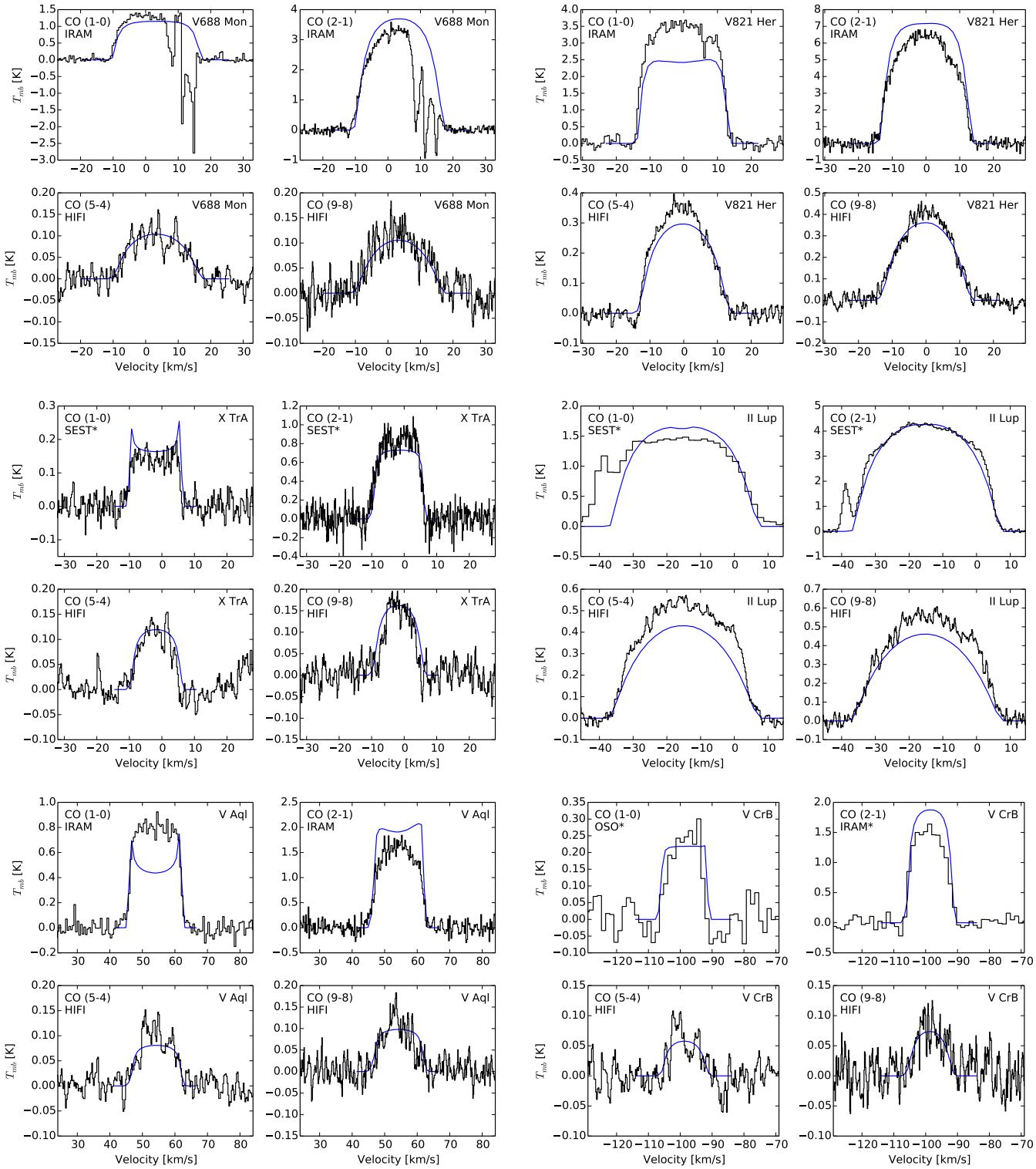

Fig. A.1. continued.

As well as plotting the model and observed CO lines, we have calculated "goodness of fit" per line in each star. This gives us an indication of which lines may be outliers or whether there are any trends across lines.

Goodness of fit for C stars is shown in Fig. A.4, for S stars in Fig. A.5, and for M stars in Fig. A.6. See Fig. 5 and Sect. 4.2 for a discussion of goodness of fit across the entire sample. A list of archival lines included in our models is given in Table C.1.

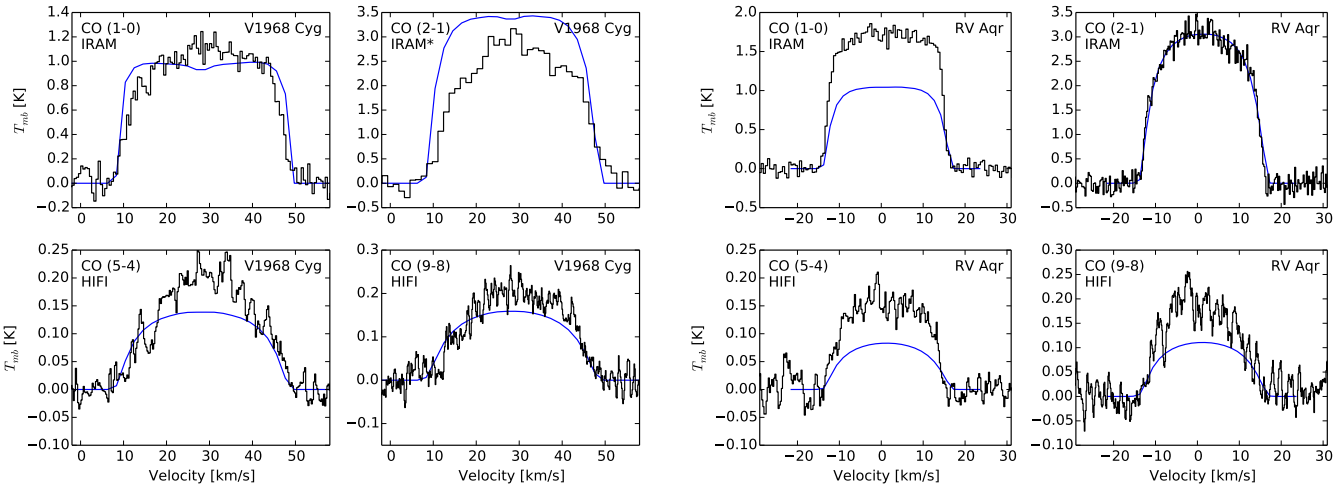

Fig. A.1. continued.

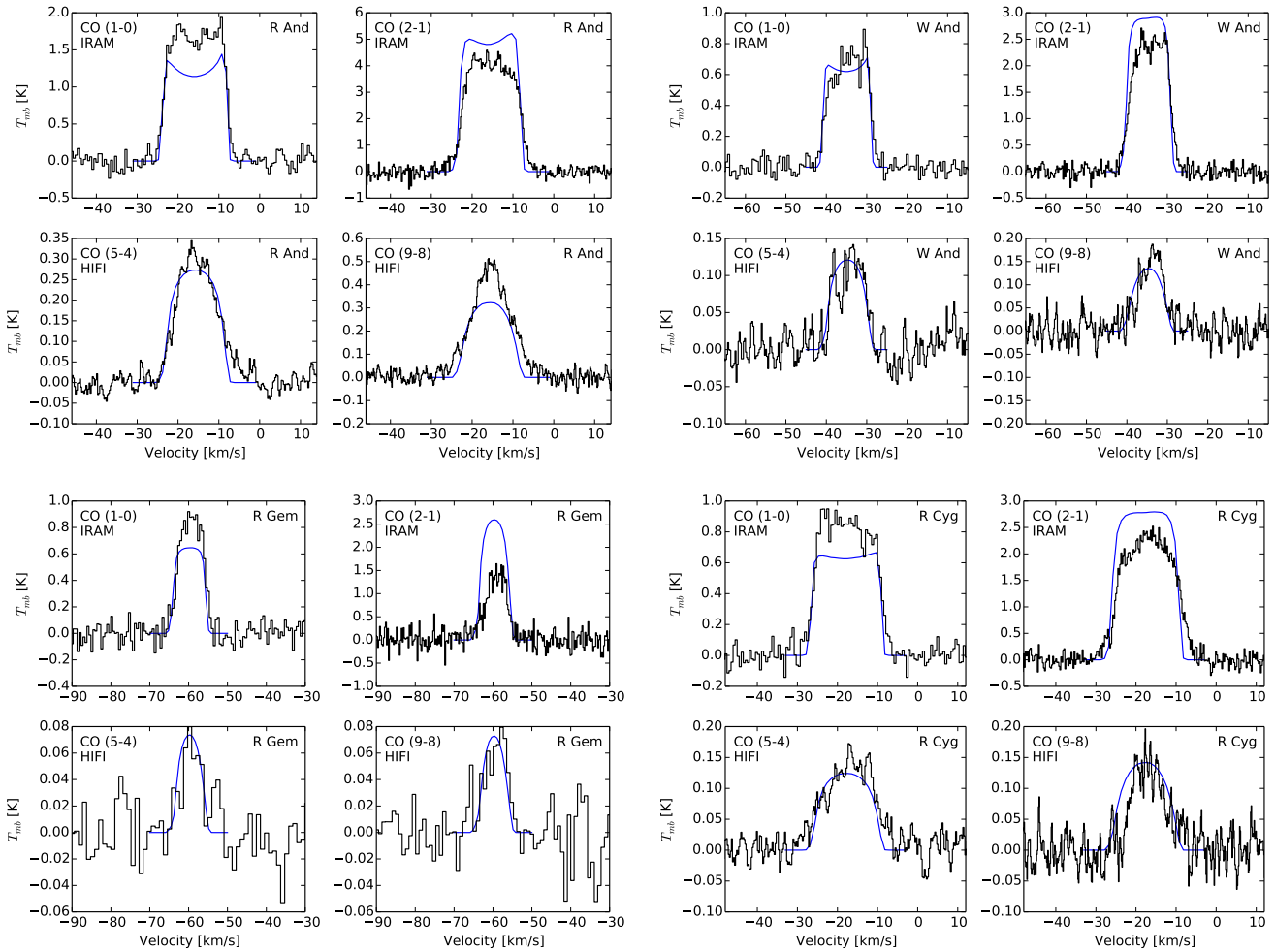

Fig. A.2. Models (blue) and observed data (black) of S stars, plotted with respect to LSR velocity.

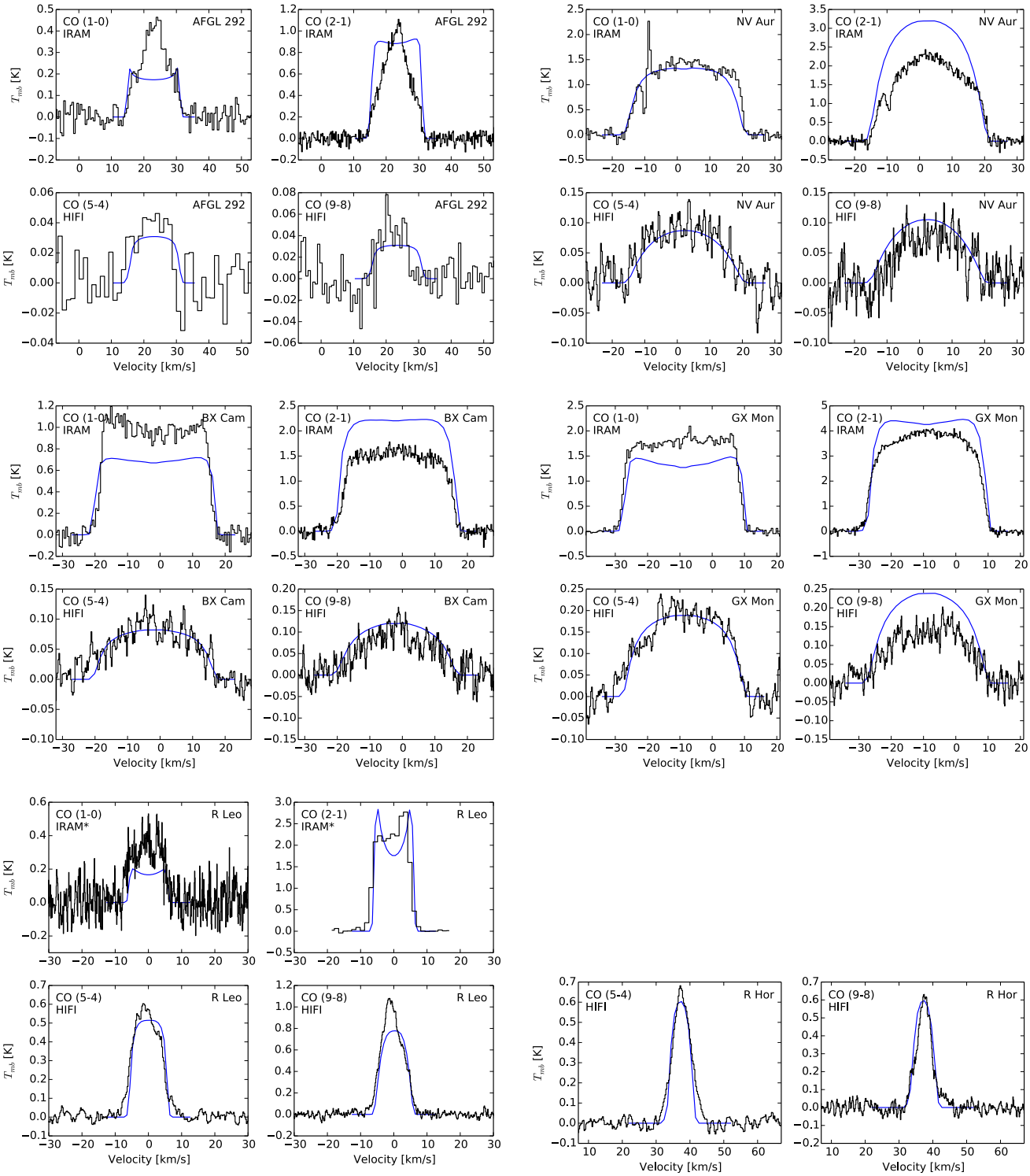

Fig. A.3. Models (blue) and observed data (black) of M stars, plotted with respect to LSR velocity. An * next to the telescope name indicates archival data is plotted.

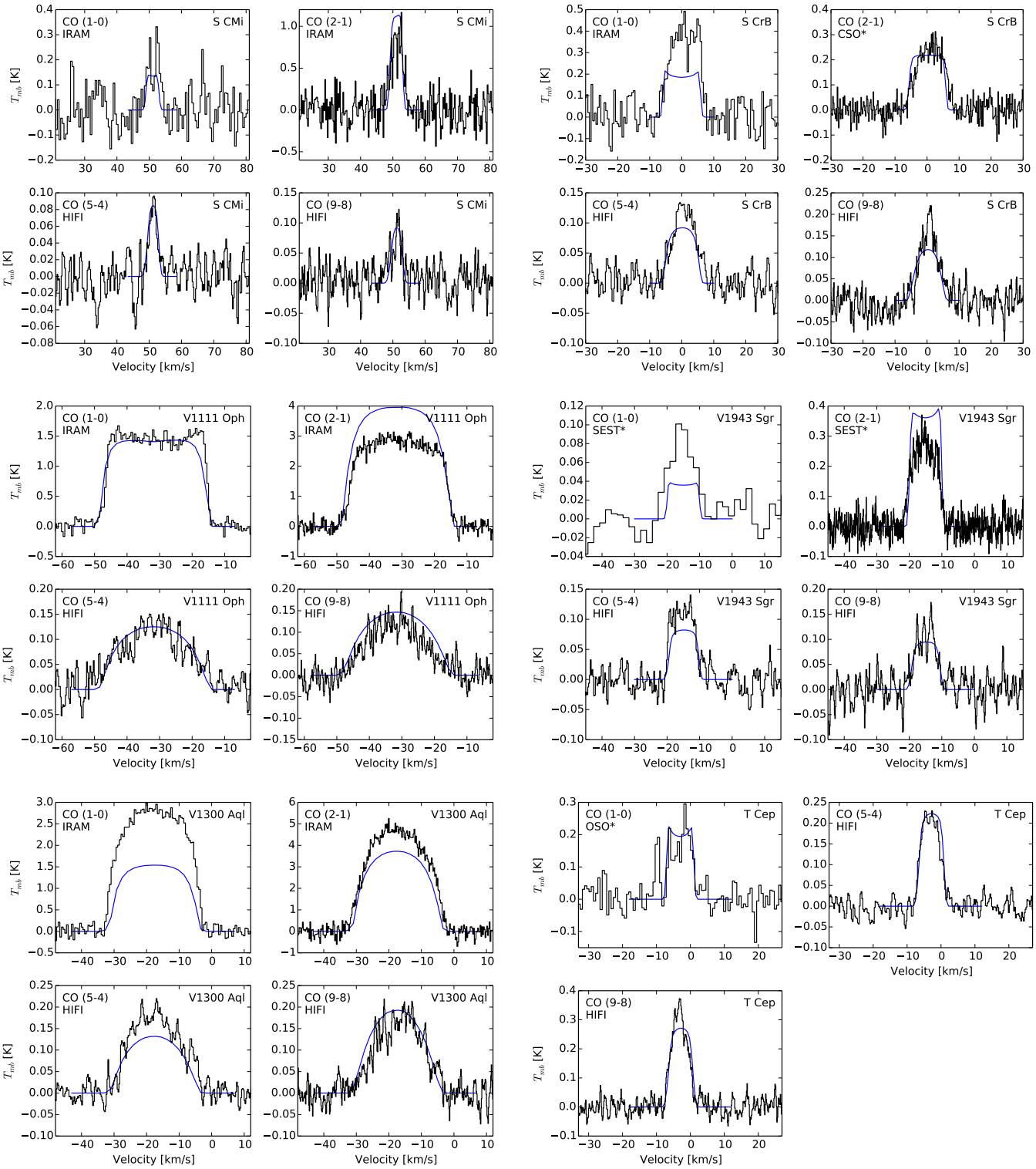

Fig. A.3. continued.

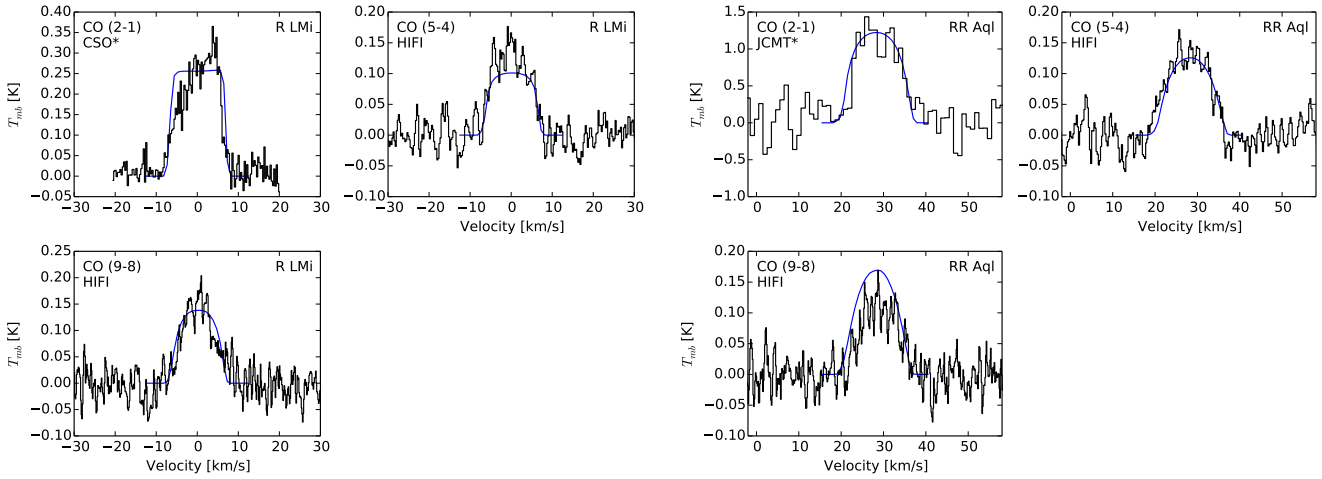

Fig. A.3. continued.

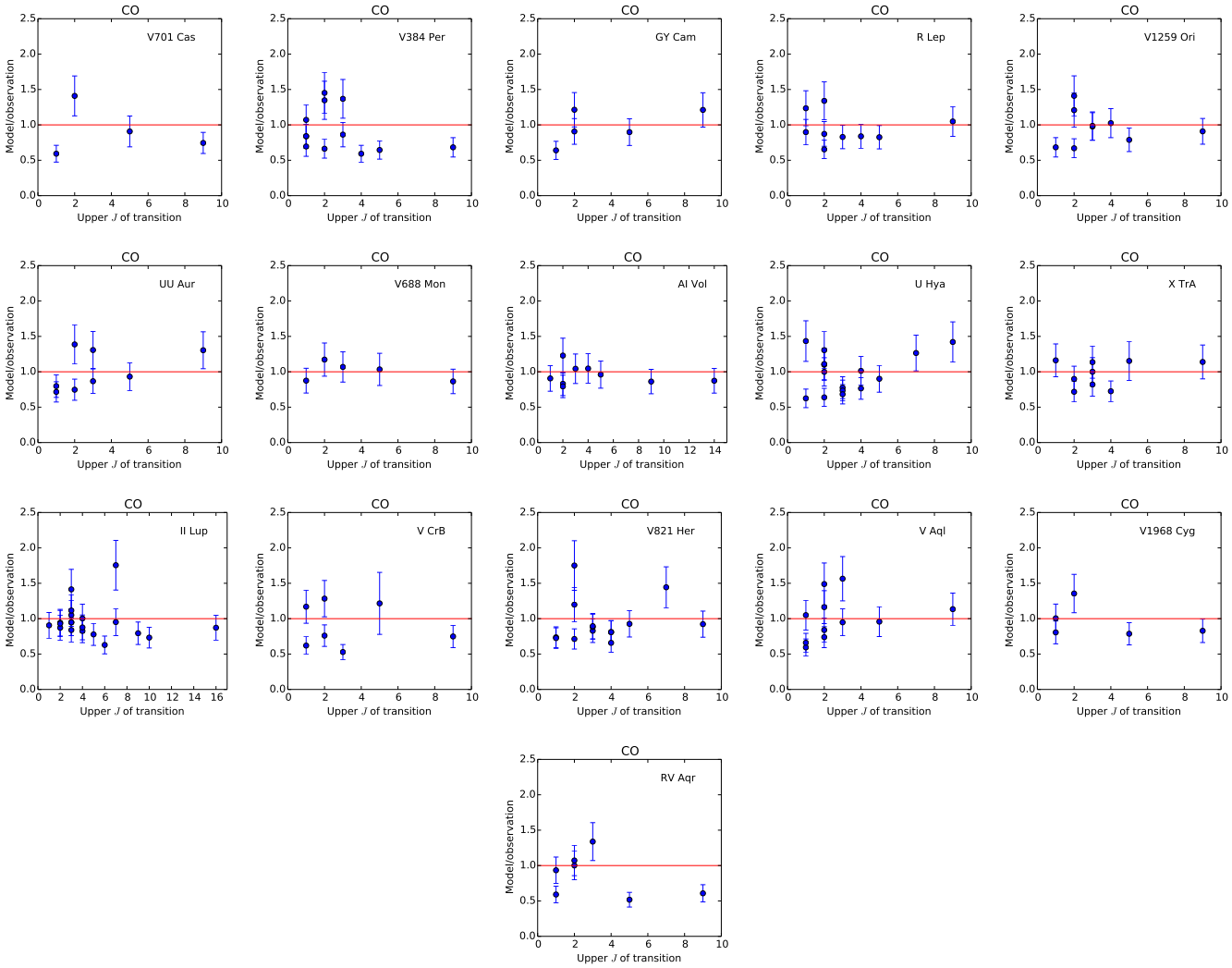

Fig. A.4. Goodness of fit as defined by model/observed intensity for C stars.

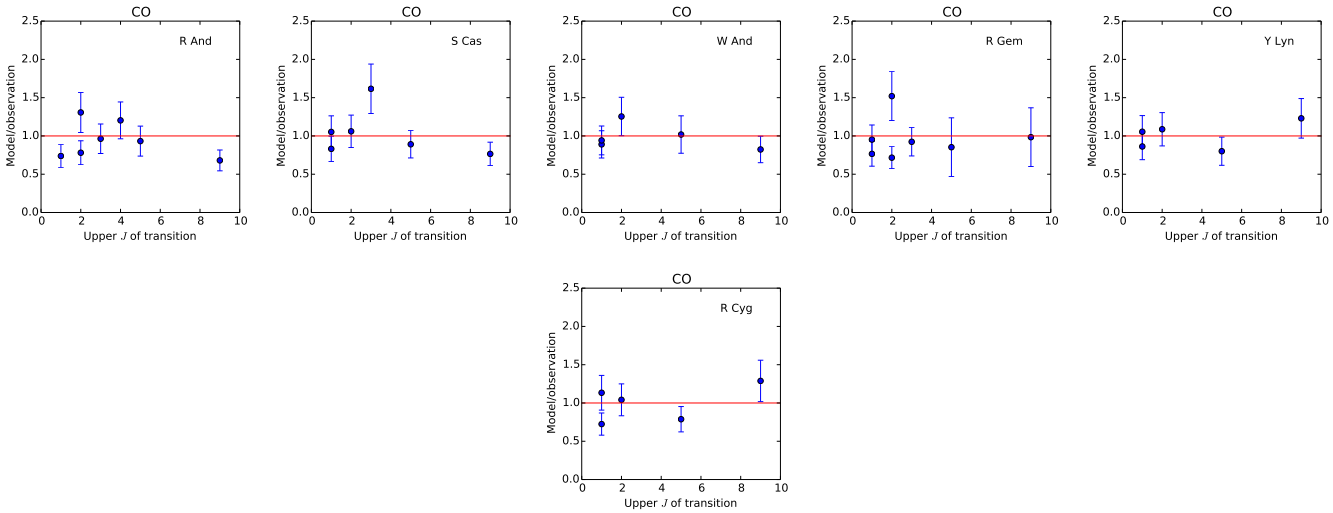

Fig. A.5. Goodness of fit as defined by model/observed intensity for S stars.

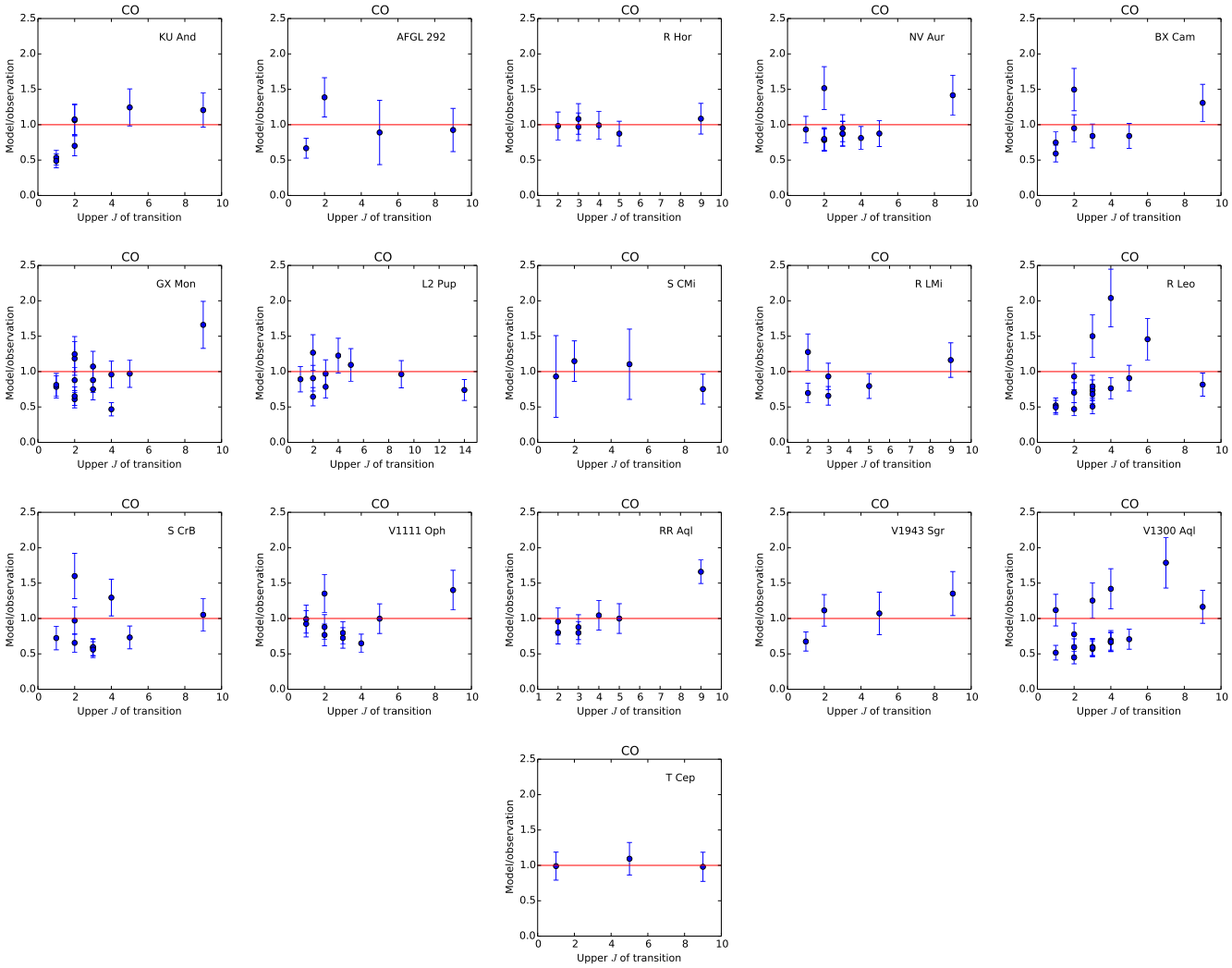

Fig. A.6. Goodness of fit as defined by model/observed intensity for M stars.

Appendix B: New observations

B.1. CO lines

Of the data described in Table 2, those stars for which we ran radiative transfer models were plotted in the body of the paper and in Appendix A. The remaining lines, which were excluded from modelling for various reasons (see discussion in Sect. 4.1) are now presented here. The C stars are plotted in Fig. B.1, the S stars are plotted in Fig. B.2 and the M stars are plotted in Fig. B.3.

In particular, the unusual line profile due to the presence of a detached shell can be seen in the C star R Scl and double-component winds are clearly evident in C star TX Psc and S stars RS Cnc and π^1 Gru.

The observation identifiers (ObsIDs) for our *Herschel* observations are listed in Table B.1.

B.2. Bonus lines

As mentioned in Sect. 2.4, we acquired some "bonus" line spectra for molecules that were observable within our target frequency ranges. In HIFI, in the same range as the CO (5 → 4) line, we detected SiO (13 → 12) at 564.249 GHz. As can be seen in Table B.2, it was mostly detected in M stars, especially those of lower mass-loss rates, which is in agreement with the trend found by González Delgado et al. (2003) and the calculations performed by Schöier et al. (2004).

Our detections are plotted in Fig. B.4. There was one detection in an S star, RS Cnc, which is the most "M-like" S star in our sample, based on optical classifications. There were also two detections in C stars: V384 Per and V821 Her. They both have mass-loss rates in the range ∼2–3 × 10^{-6} $M_\odot$ yr^{-1}, putting them in the mid-to-high mass-loss rate range. They are located at 560 and 600 pc respectively, making them two of the nearest C stars in the higher mass-loss rate range (>10^{-6} $M_\odot$ yr^{-1}). This could be why they had (weak) detections, while there were no detections in other C stars. The two C stars are among the sample modelled in SiO by Schöier et al. (2006). These authors used observations of SiO lines from J = 8 → 7 down to J = 2 → 1 and there are six overlapping stars between their sample and the one in this paper, leaving four stars (AI Vol, II Lup, RV Aqr, and R Lep) detected in the lower-J SiO lines but not in the higher-J HIFI line.

Covered by our IRAM observations was the ^{13}CO (1 → 0) line at 110.201 GHz. The integrated intensities for these detections are given in Table B.2 and the observations are plotted in Fig. B.5. The ^{13}CO (1 → 0) line seems to have been most reliably detected in higher mass-loss rate sources across the three chemical types. It was not detected at all in stars with mass-loss rates ∼10^{-8}–10^{-7} $M_\odot$ yr^{-1} (note, however, that we are only dealing with two stars in this range) and was detected increasingly often for increasing mass-loss rates across chemical types.

The SiS (6 → 5) line at 108.924 GHz was also detected in seven C stars, five M stars and no S stars. The integrated intensities are listed in Table B.2 and the spectra are plotted in Fig. B.6. The C stars with detections were all in the mass-loss rate range ∼10^{-6} to 10^{-5} $M_\odot$ yr^{-1}, with no detections for lower mass-loss rate objects and only one detection out of the two highest mass-loss rate C stars observed. Of the M stars, SiS was also detected in the higher mass-loss rate objects, but not in the highest mass-loss rate star, V1111 Oph. This trend suggests that SiS is more readily formed – or at least more readily detectable – in sources of intermediate mass-loss rate, around the range ∼10^{-6} to 10^{-5} $M_\odot$ yr^{-1}.

CN lines were covered by both HIFI and IRAM observations. The CN ($5_{9/2}$ → $4_{7/2}$) and ($5_{11/2}$ → $4_{9/2}$) line groups with rest frequencies taken as 566.693 GHz and 566.947 GHz were covered in the observing range for CO (5 → 4) and were detected in a handful of C stars. Our IRAM observations covered the CN N = 1 → 0 lines at 113.123 GHz and 113.488 GHz for the ($1_{1/2}$ − $0_{1/2}$) and ($1_{3/2}$ − $0_{1/2}$) line groups, respectively, and the CN N = 2 → 1 lines at 226.617 GHz, 226.874 GHz and 226.360 GHz for the ($2_{3/2}$ − $1_{1/2}$), ($2_{3/2}$ − $1_{3/2}$), and ($2_{5/2}$ − $1_{3/2}$) line groups, respectively. The hyperfine structure of the low-N CN lines can be seen particularly clearly. The integrated intensities of each line group are given in Table B.3 and the observations themselves are plotted in Fig. B.7.

Low-N CN lines were detected in all of the observed C stars. Not all lines were detected in all stars, however. The lowest mass-loss rate star, U Hya, did not yield a clear detection of the ($1_{1/2}$−$0_{1/2}$) or ($2_{3/2}$−$1_{3/2}$) groups, although the remaining lines, including the ($5_{9/2}$ → $4_{7/2}$) and ($5_{11/2}$ → $4_{9/2}$) groups were clearly seen. The ($2_{3/2}$−$1_{3/2}$) was also not detected in V701 Cas, V1259 Ori, V688 Mon, or V821 Her, all of which are relatively high mass-loss rate objects with $\dot{M}$ ∼ 10^{-6}–10^{-5} $M_\odot$ yr^{-1}. One S star, S Cas, was also detected in CN, in the ($1_{3/2}$−$0_{1/2}$), ($2_{3/2}$−$1_{1/2}$), ($2_{3/2}$−$1_{3/2}$), and ($2_{5/2}$−$1_{3/2}$) line groups. S Cas is the highest mass-loss rate and expansion velocity S star and, from its optical classification of S4/6e, is on the higher C/O end of the S star scale.

The last bonus line we detected was HC_3N (12 → 11) at 109.174 GHz. The integrated intensities for the detections are listed in Table B.3 and the spectra are plotted in Fig. B.6. HC_3N was only detected in C stars and not in the three lowest mass-loss rate objects with mass-loss rates below 10^{-6} $M_\odot$ yr^{-1}. This is probably due to a higher density of available carbon to form this (simple) carbon-chain molecule in the higher mass-loss rate C stars.

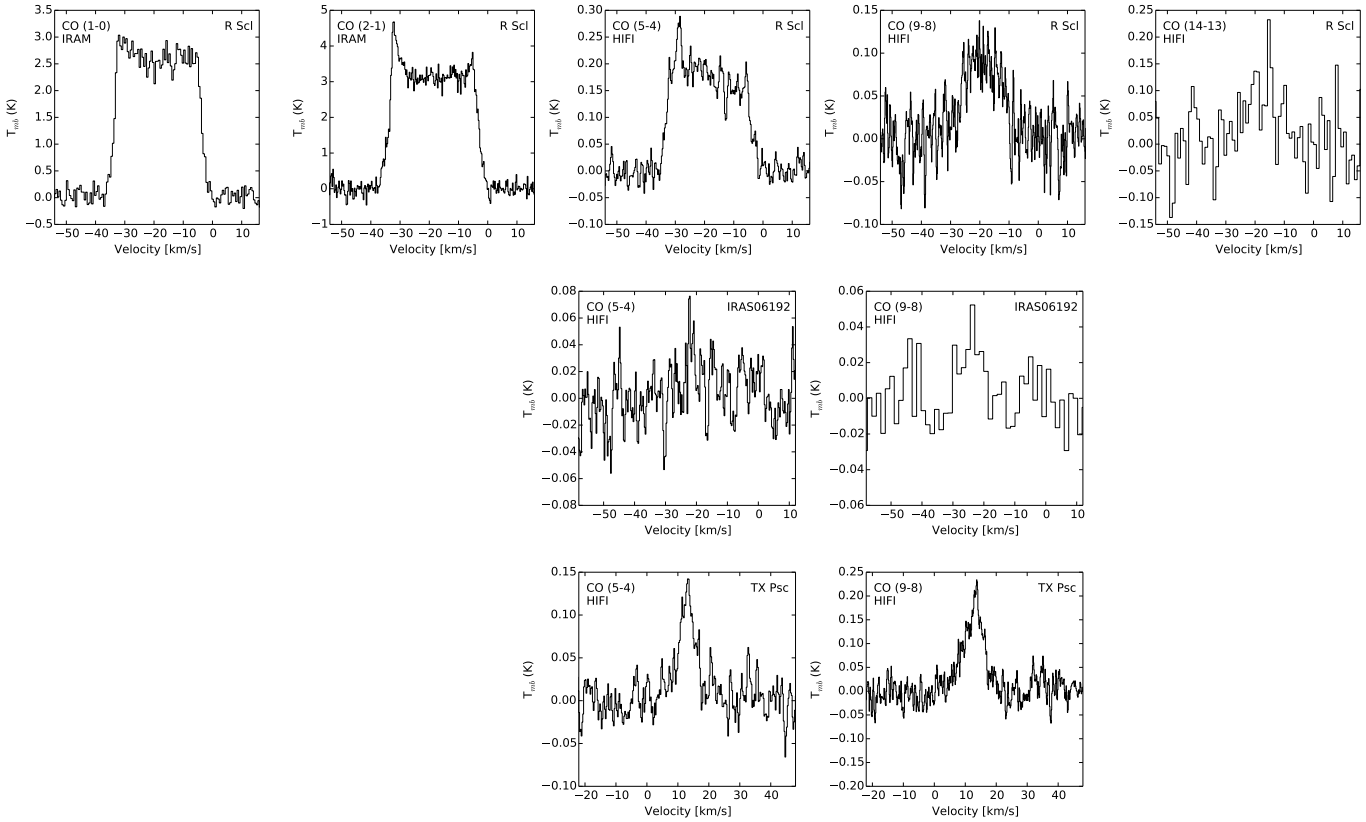

Fig. B.1. New data from HIFI and IRAM for C stars not modelled in this paper, plotted with respect to LSR velocity.

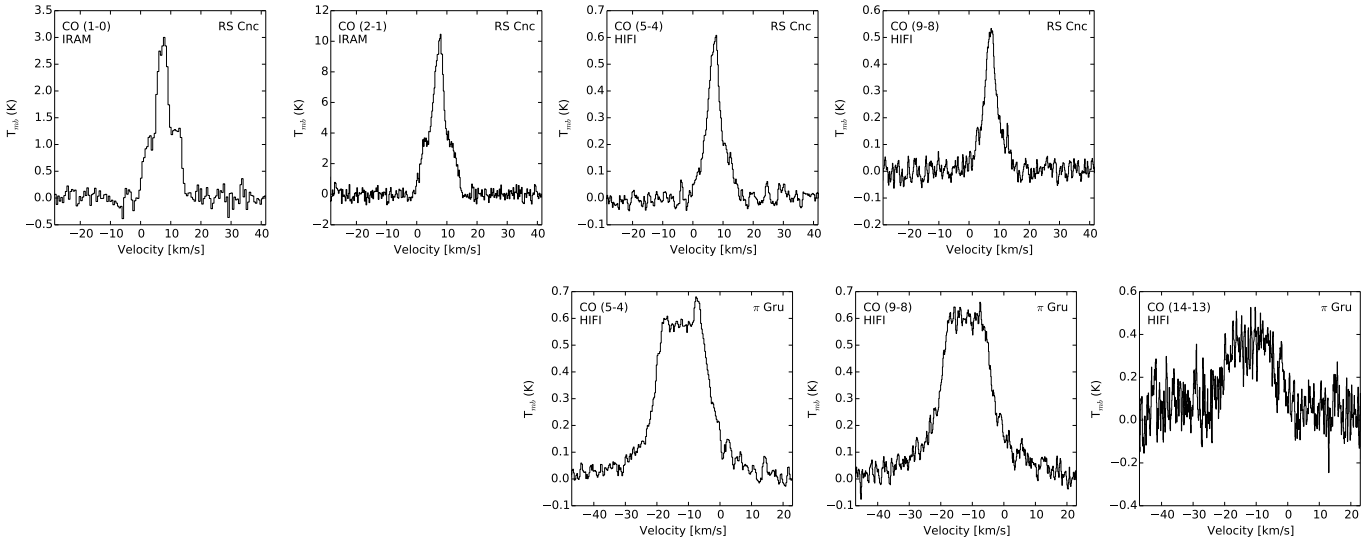

Fig. B.2. New data from HIFI and IRAM for S stars not modelled in this paper, plotted with respect to LSR velocity.

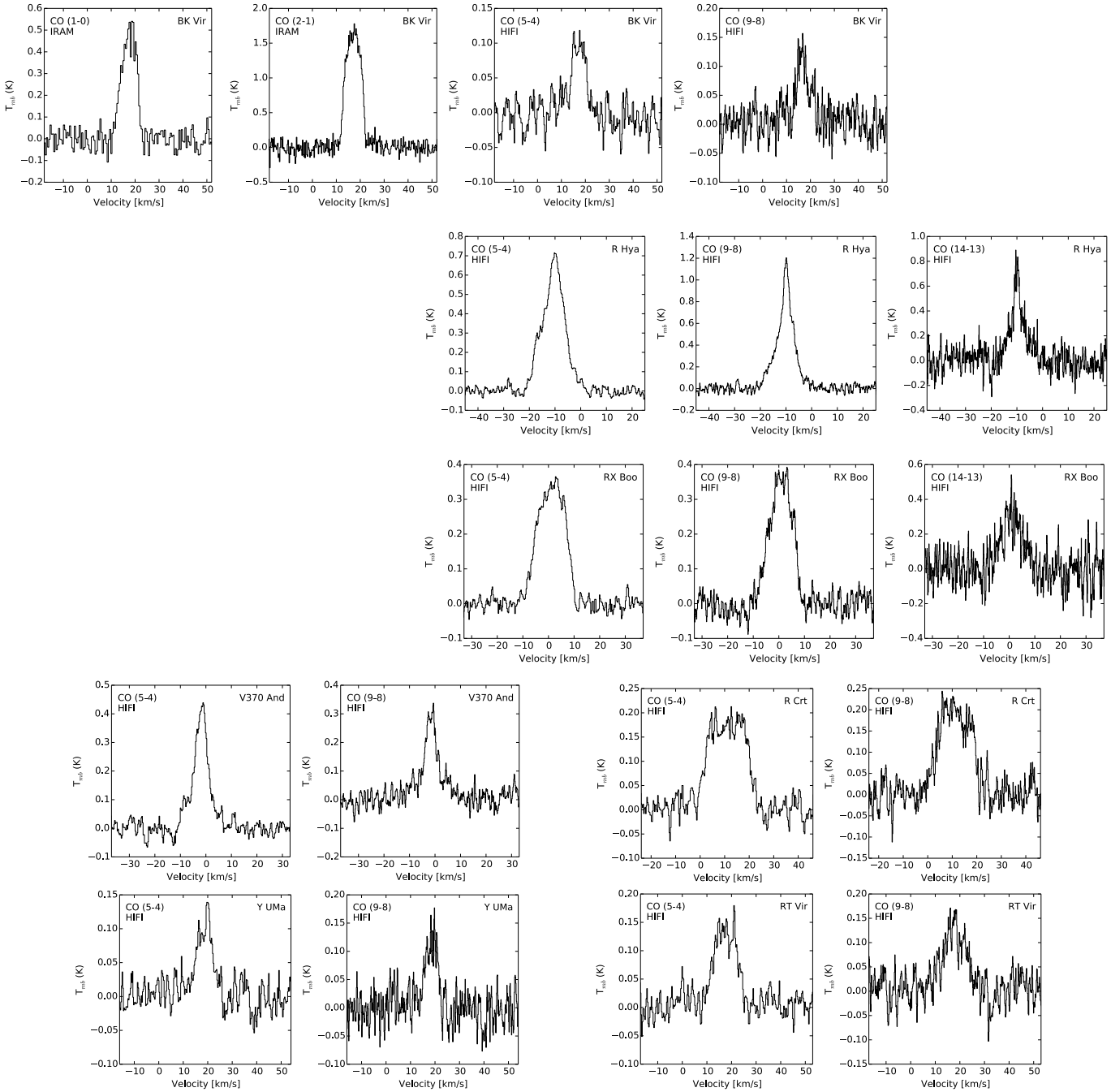

Fig. B.3. New data from HIFI and IRAM for M stars not modelled in this paper, plotted with respect to LSR velocity.

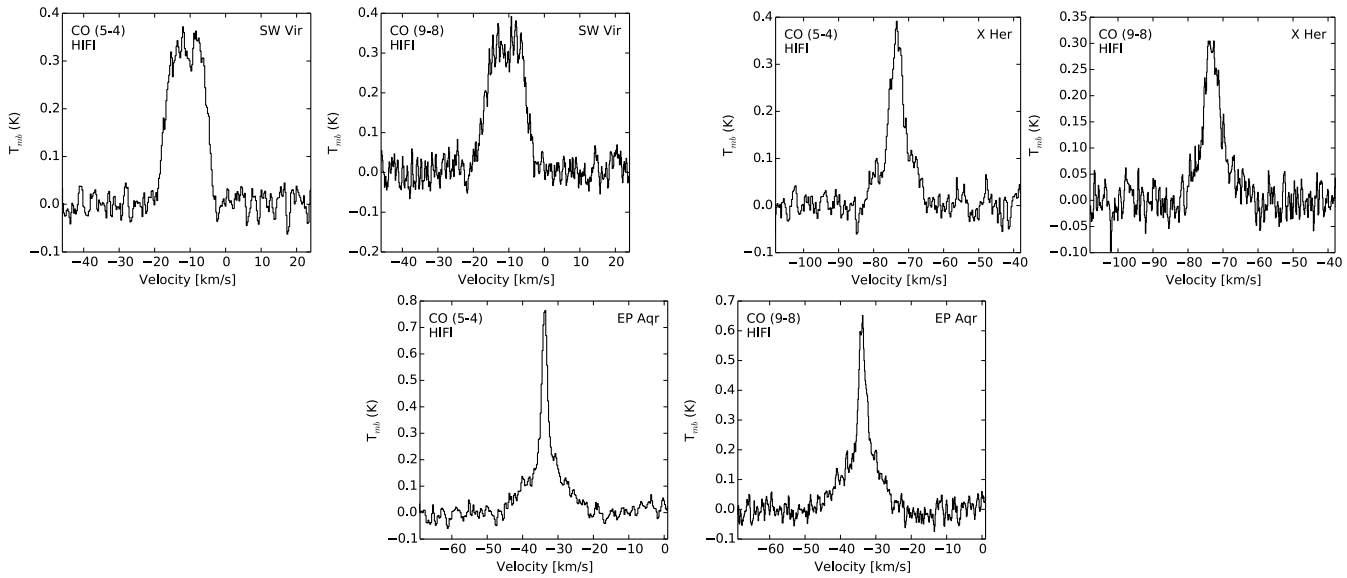

Fig. B.3. continued.

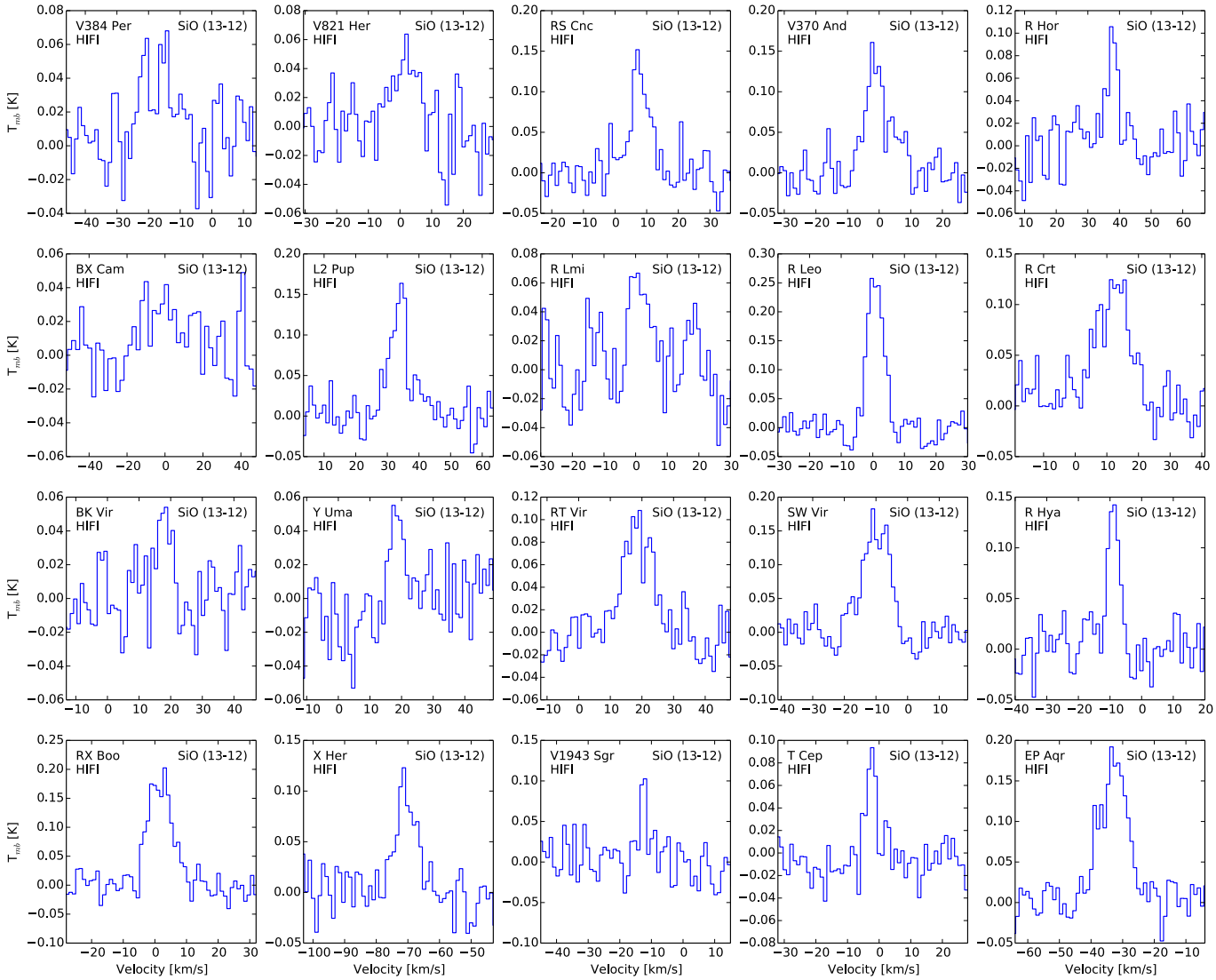

Fig. B.4. New SiO data from HIFI, plotted with respect to LSR velocity.

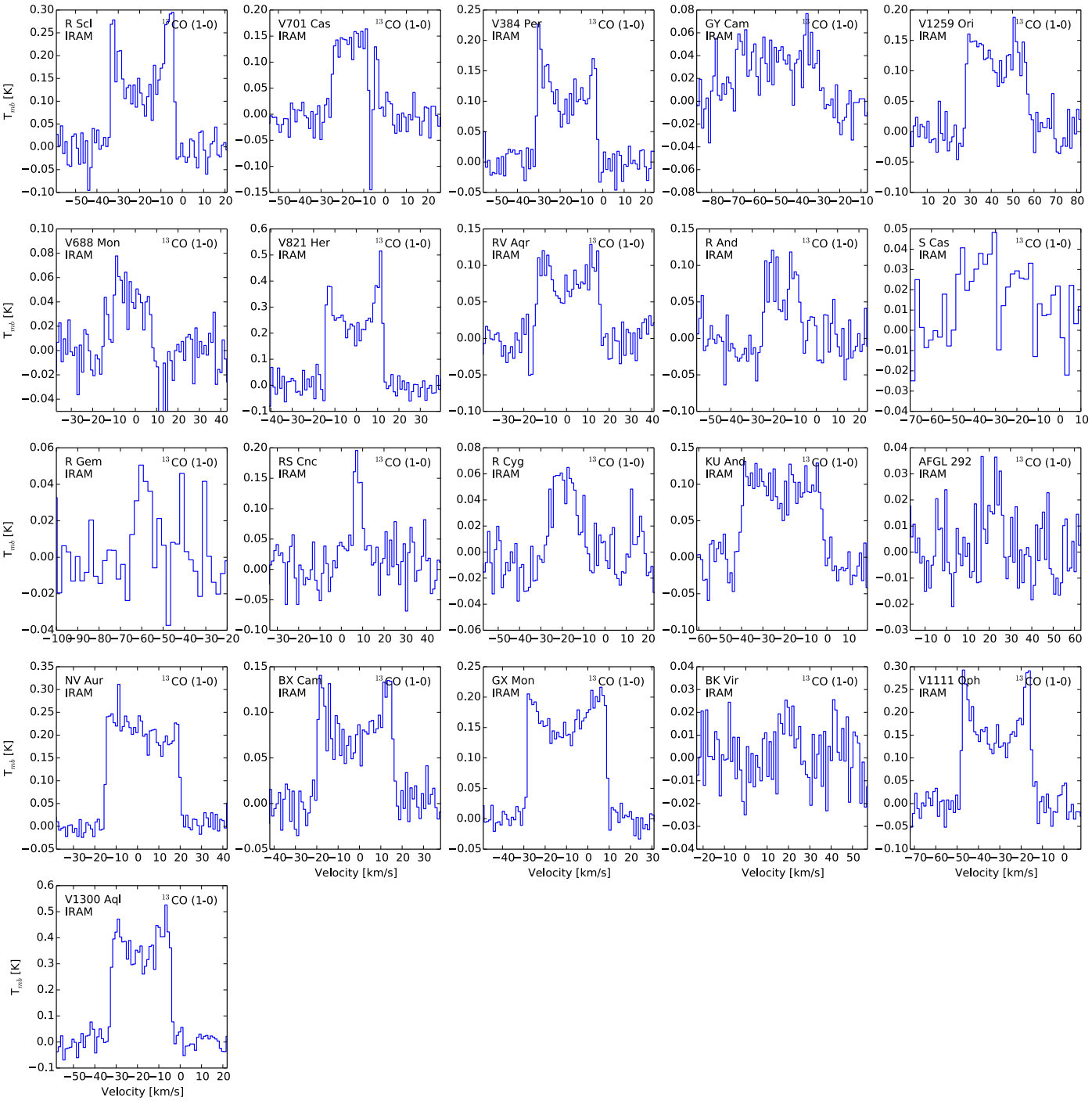

Fig. B.5. New ^{13}CO data from IRAM, plotted with respect to LSR velocity.

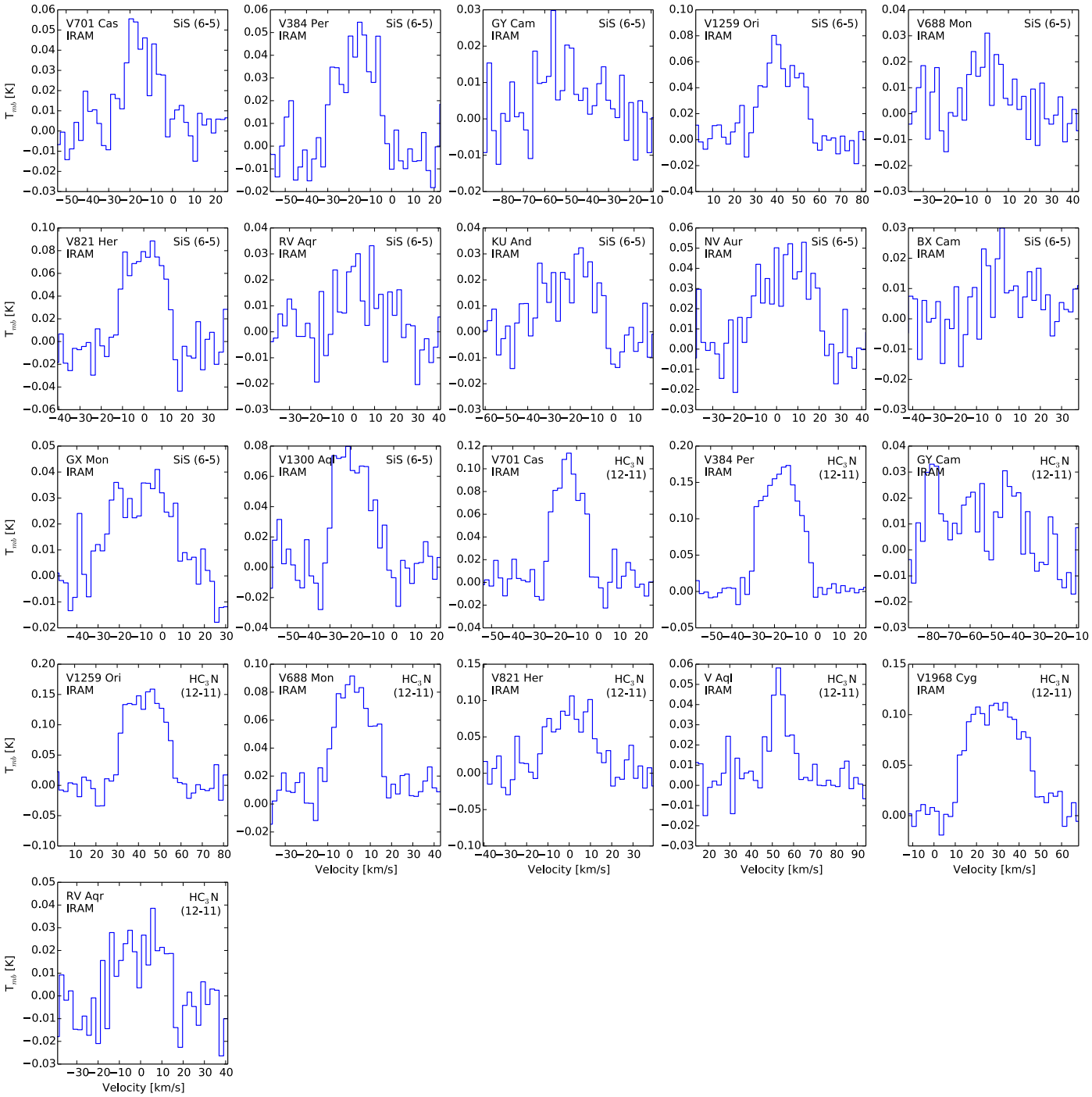

Fig. B.6. New SiS and HC_3N data from IRAM, plotted with respect to LSR velocity. Note that the peak at ~–80 km s^{-1} in the GY Cam H_3CN spectrum is an artefact and not part of the H_3CN line.

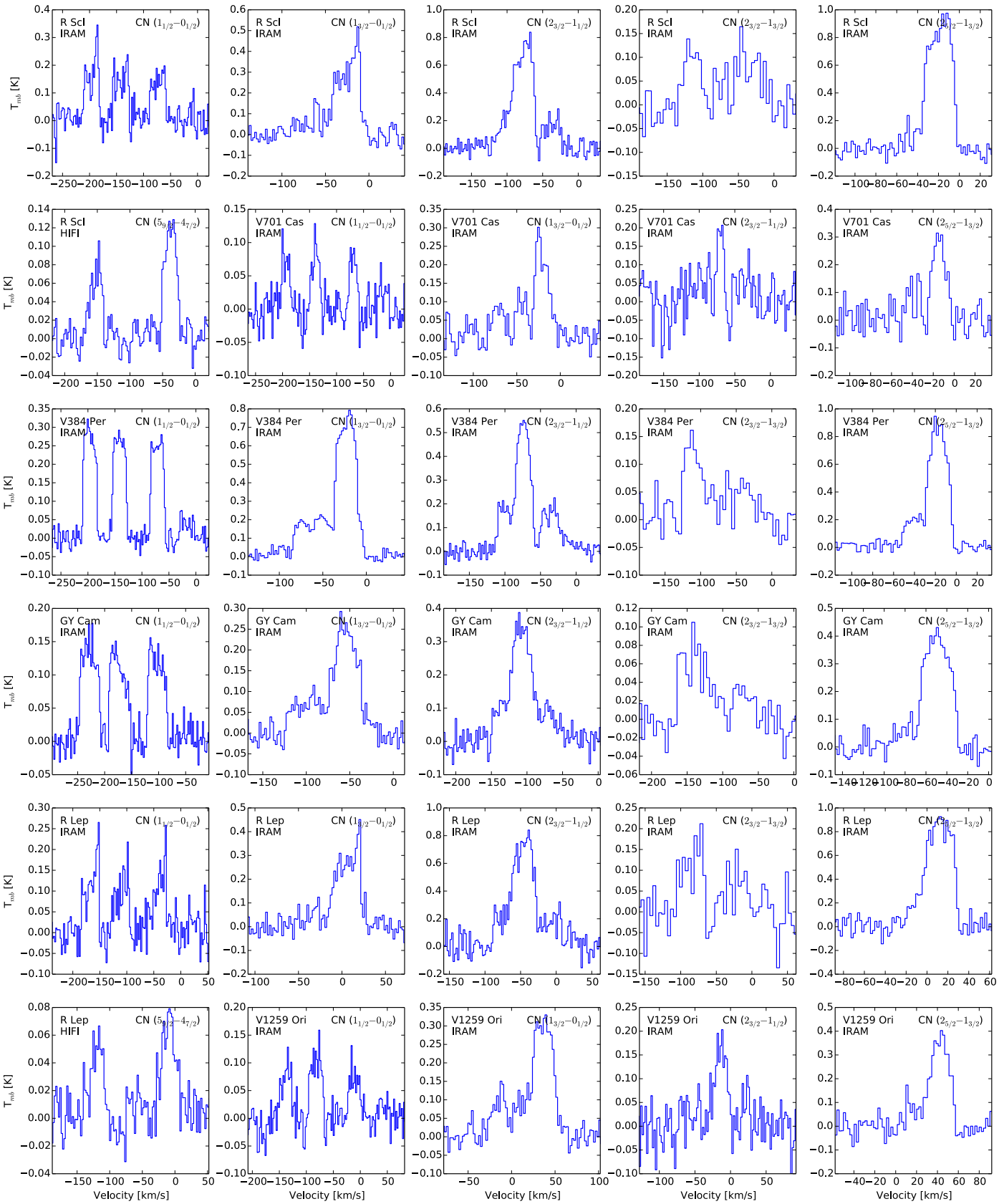

Fig. B.7. New CN data from HIFI and IRAM, plotted with respect to LSR velocity of the reddest component. In the case of the HIFI lines, both the ($5_{9/2} \rightarrow 4_{7/2}$) and ($5_{11/2} \rightarrow 4_{9/2}$) lines are plotted together at the rest frequency of the former.

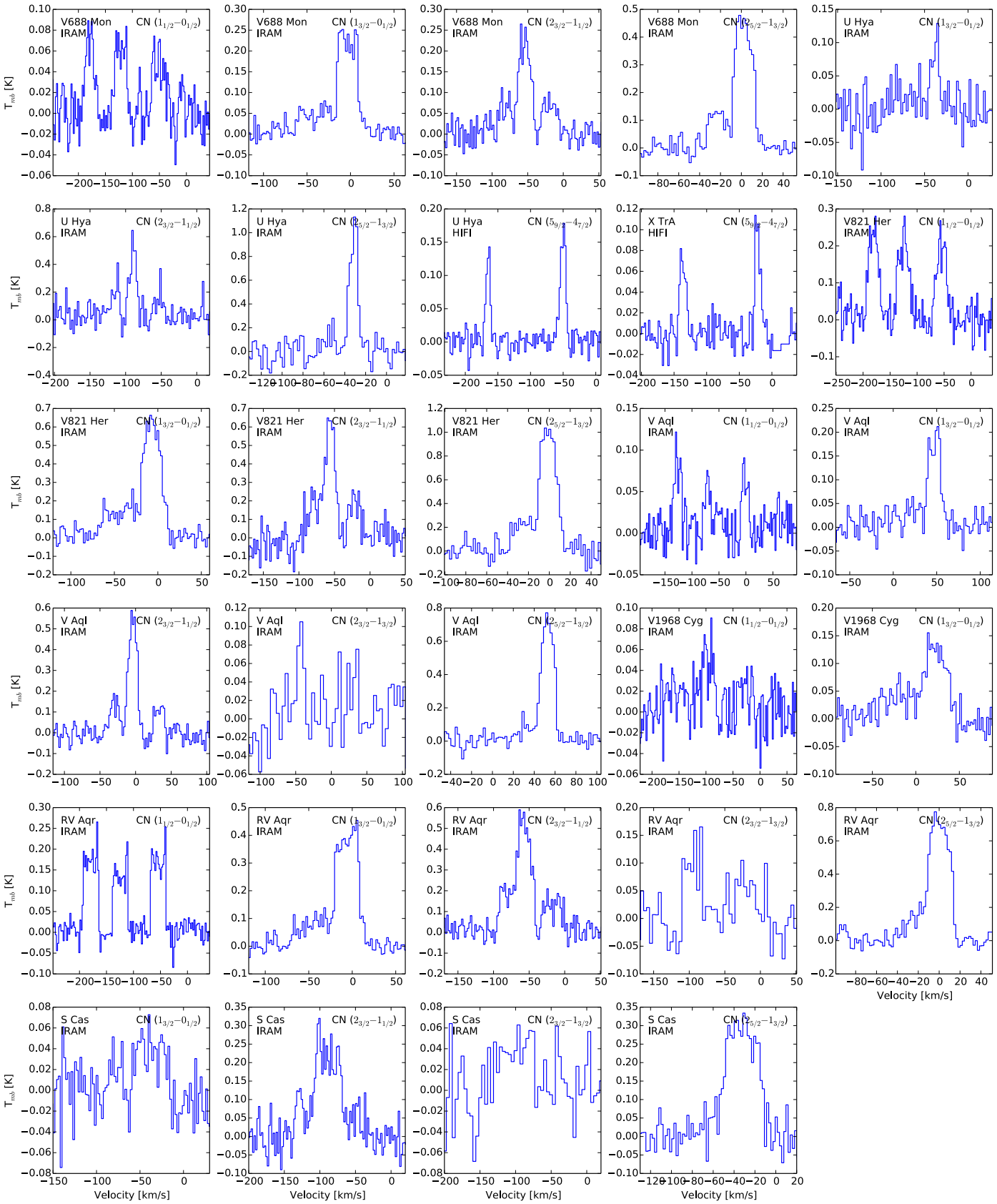

Fig. B.7. continued.

Table B.1. ObsIDs for *Herschel* observations.

Source	ObsID CO(5 → 4)	ObsID CO(9 → 8)	ObsID CO(14 → 13)
V1968 Cyg	1342210073	1342221424	...
AFGL 292	1342200903	1342213353	...
V701 Cas	1342201532	1342227533	...
V1259 Ori	1342218903	1342227530	...
V688 Mon	1342218902	1342229929	...
BK Vir	1342210683	1342212125	...
BX Cam	1342230363	1342227532	...
EP Aqr	1342210079	1342220501	...
GX Mon	1342228562	1342228602	...
IRAS 06192+4657	1342230362	1342227531	...
AI Vol	1342204015	1342210044	1342229787
	1342200911	...	...
II Lup	1342202049	1342227540	...
V1111 Oph	1342230369	1342229924	...
KU And	1342200923	1342213361	...
V370 And	1342201528	1342213354	...
V384 Per	1342204006	1342227534	...
	1342204007	1342216333	...
NV Aur	1342217689	1342218627	...
GY Cam	1342214328	1342218626	...
V1300 Aql	1342210080	1342216809	...
L_2 Pup	1342202055	1342210049	1342231773
π Gru	1342210084	1342210043	1342220504
R And	1342200924	1342213362	...
R Crt	1342210087	1342212121	...
R Cyg	1342200920	1342210034	...
R Gem	1342228561	1342228601	...
R Hor	1342200910	1342213350	...
R Hya	1342200913	1342212120	1342223432
R LMi	1342220512	1342220498	...
R Leo	1342210684	1342220493	...
R Lep	1342214326	1342216330	...
R Scl	1342210695	1342213347	1342221454
	1342200909	...	...
RR Aql	1342216806	1342216808	...
RS Cnc	1342220513	1342220497	...
RT Vir	1342200915	1342212126	...
RV Aqr	1342210078	1342218413	...
RX Boo	1342200916	1342212129	1342223433
S Cas	1342204009	1342213358	...
	1342201533	...	...
S CMi	1342220514	1342220496	...
S CrB	1342200917	1342212128	...
SW Vir	1342200914	1342212124	...
T Cep	1342201535	1342210666	...
TX Psc	1342210686	1342222348	...
U Hya	1342210088	1342212122	...
UU Aur	1342230361	1342229926	...
V Aql	1342230383	1342229921	...
V CrB	1342200918	1342214438	...
V1943 Sgr	1342216804	1342216812	...
V821 Her	1342230368	1342215900	...
W And	1342201527	1342213355	...
X Her	1342200919	1342210033	...
X TrA	1342202053	1342216329	...
Y Lyn	1342230360	1342229925	...
Y Uma	1342210067	1342212127	...

Table B.2. IRAM and HIFI ^{13}CO, SiO and SiS line observations.

Star	^{13}CO (1 → 0) [K km s^{-1}]	SiO (13 → 12) [K km s^{-1}]	SiS (6 → 5) [K km s^{-1}]
C Stars			
R Scl	4.7 (0.4)	<0.1	<0.4
V701 Cas	* 2.7 (0.2)	<0.22	0.94 (0.15)
V384 Per	3.9 (0.2)	0.73 (0.18)	0.77 (0.14)
GY Cam	2.0 (0.2)	<0.20	0.38 (0.15)
V1259 Ori	3.5 (0.2)	<0.21	1.40 (0.13)
V688 Mon	* 1.5 (0.2)	<0.19	0.41 (0.12)
V821 Her	7.7 (0.4)	0.29 (0.16)	1.33 (0.22)
RV Aqr	2.2 (0.2)	<0.13	0.39 (0.14)
S Stars			
R And	0.83 (0.29)	<0.16	<0.3
S Cas	1.3 (0.2)	<0.18	<0.2
R Gem	0.34 (0.26)	<0.23	<0.3
RS Cnc	1.0 (0.3)	0.90 (0.16)	<0.3
R Cyg	0.41 (0.21)	<0.16	<0.2
M Stars			
KU And	3.7 (0.2)	<0.16	0.55 (0.15)
V370 And	...	1.07 (0.22)	...
AFGL 292	0.16 (0.10)	<0.23	<0.1
R Hor	...	0.41 (0.18)	...
NV Aur	7.9 (0.2)	<0.13	1.25 (0.12)
BX Cam	2.9 (0.2)	0.85 (0.22)	0.40 (0.11)
GX Mon	6.2 (0.2)	<0.18	1.04 (0.12)
L_2 Pup	...	1.13 (0.19)	...
R LMi	...	0.54 (0.22)	...
R Leo	...	1.46 (0.18)	...
R Crt	...	1.73 (0.17)	...
BK Vir	0.04 (0.13)	0.29 (0.17)	<0.1
Y UMa	...	0.10 (0.18)	...
RT Vir	...	0.87 (0.18)	...
SW Vir	...	1.50 (0.22)	...
R Hya	...	0.72 (0.18)	...
RX Boo	...	1.63 (0.20)	...
X Her	...	0.79 (0.27)	...
V1111 Oph	5.6 (0.3)	<0.19	<0.3
V1943 Sgr	...	0.37 (0.17)	...
V1300 Aql	11.0 (0.4)	<0.15	1.53 (0.22)
T Cep	...	0.32 (0.17)	...
EP Aqr	...	2.00 (0.21)	...

Notes. The value in brackets after the flux gives the integrated noise rms. An ellipsis (...) indicates that the line was not observed for the indicated star. * indicates that flux has been corrected for ISM emission.

Table B.3. HIFI and IRAM CN and H_3CN line group observations.

Star	CN							HC_3N
	$1_{1/2} \rightarrow 0_{1/2}$ [K km s^{-1}]	$1_{3/2} \rightarrow 0_{1/2}$ [K km s^{-1}]	$2_{3/2} \rightarrow 1_{1/2}$ [K km s^{-1}]	$2_{3/2} \rightarrow 1_{3/2}$ [K km s^{-1}]	$2_{5/2} \rightarrow 1_{3/2}$ [K km s^{-1}]	$5_{9/2} \rightarrow 4_{7/2}$ [K km s^{-1}]	$5_{11/2} \rightarrow 4_{9/2}$ [K km s^{-1}]	$12 \rightarrow 11$ [K km s^{-1}]
R Scl	15.6 (1.0)	13.2 (1.0)	31.4 (0.9)	7.1 (0.9)	25.2 (0.9)	3.0 (0.1)	1.7 (0.1)	<1.0
V701 Cas	3.7 (0.3)	8.5 (0.3)	5.0 (0.4)	<0.4	6.3 (0.4)	<0.2	<0.2	1.76 (0.17)
V384 Per	21.6 (0.2)	28.4 (0.2)	21.9 (0.3)	7.0 (0.3)	23.3 (0.3)	<0.2	<0.2	3.72 (0.12)
GY Cam	13.8 (0.2)	10.9 (0.2)	16.2 (0.3)	3.7 (0.3)	12.9 (0.3)	<0.2	<0.2	0.69 (0.17)
R Lep	11.8 (0.4)	11.7 (0.4)	37.2 (0.6)	6.8 (0.6)	29.5 (0.6)	2.0 (0.1)	1.2 (0.1)	<0.4
V1259 Ori	6.1 (0.2)	12.6 (0.2)	4.6 (0.3)	<0.3	8.9 (0.3)	<0.2	<0.2	3.13 (0.16)
V688 Mon	4.2 (0.3)	8.7 (0.3)	8.1 (0.2)	<0.2	11.6 (0.2)	<0.2	<0.2	2.40 (0.15)
U Hya	<0.4	1.4 (0.4)	17.1 (1.0)	<1.0	11.6 (1.0)	1.8 (0.2)	1.1 (0.2)	<0.4
X TrA	...	...	...	...	...	1.0 (0.2)	0.7 (0.2)	...
V821 Her	15.8 (0.5)	22.6 (0.5)	17.1 (0.7)	<0.7	25.2 (0.7)	<0.2	<0.2	2.26 (0.24)
V Aql	4.4 (0.2)	4.9 (0.2)	10.6 (0.3)	2.4 (0.3)	13.0 (0.3)	<0.1	<0.1	0.26 (0.08)
V1968 Cyg	3.0 (0.3)	5.6 (0.3)	...	...	...	<0.2	<0.2	1.06 (0.14)
RV Aqr	14.7 (0.2)	15.7 (0.2)	22.2 (0.4)	4.7 (0.4)	20.2 (0.4)	<0.1	<0.1	0.28 (0.15)
S Cas	<0.3	1.4 (0.3)	11.8 (0.5)	2.4 (0.5)	11.6 (0.5)	<0.2	<0.2	<0.3

Notes. The value in brackets after the flux gives the integrated noise rms. An ellipsis (...) indicates that the line was not observed for the indicated star. An * indicates the line was detected but contaminated by an artefact and the integrated intensity cannot be relied upon.

Appendix C: Supplementary line data

As discussed in Sect. 2.3, we included substantial archival data in our modelling procedure to find the models which best fit the widest range of data possible. The archival data we used to constrain our models is listed in Table C.1.

Table C.1. Archival data of other CO observations of the stars used in our modelling.

Star	Transition	I_{mb} [K km s^{-1}]	Telescope	Reference
C Stars				
V384 Per	1 → 0	52.7	IRAM	Olofsson et al. (1993)
	1 → 0	7.8*	NRAO	Schöier & Olofsson (2001)
	1 → 0	25.5*	OSO	Olofsson et al. (1993)
	2 → 1	83.6	IRAM	Olofsson et al. (1993)
	2 → 1	61.9	JCMT	Schöier & Olofsson (2001)
	3 → 2	32.8	CSO	Knapp et al. (1998)
	3 → 2	40.1	JCMT	Schöier & Olofsson (2001)
	4 → 3	78.7	JCMT	H. Olofsson, (priv. comm.)
GY Cam	2 → 1	14.3	CSO	Knapp et al. (1998)
R Lep	1 → 0	6.2	SEST	Olofsson et al. (1993)
	2 → 1	27.6	APEX	Pointing Catalogue
	2 → 1	18.1	SEST	Olofsson et al. (1993)
	3 → 2	32.3	APEX	Pointing Catalogue
	4 → 3	36.6	APEX	Pointing Catalogue
V1259 Ori	2 → 1	36.3	APEX	Pointing Catalogue
	2 → 1	16.5	CSO	Knapp et al. (1998)
	3 → 2	32.5	APEX	Pointing Catalogue
	3 → 2	32.2	APEX	Archive
	4 → 3	30.4	APEX	Pointing Catalogue
UU Aur	1 → 0	18.8	IRAM	Olofsson et al. (1993)
	1 → 0	7.9	OSO	Olofsson et al. (1993)
	2 → 1	15.0	APEX	Pointing Catalogue
	2 → 1	39.0	IRAM	Olofsson et al. (1993)
	3 → 2	21.6	APEX	Pointing Catalogue
	3 → 2	22.7	JCMT	H. Olofsson, (priv. comm.)
V688 Mon	3 → 2	15.4*	CSO	Knapp et al. (1998)
AI Vol	1 → 0	25.57	SEST	Woods et al. (2003)
	2 → 1	56.5	APEX	Pointing Catalogue
	2 → 1	59.1	APEX	Hans pointing data
	2 → 1	50.00	SEST	Woods et al. (2003)
	3 → 2	57.8	APEX	Pointing Catalogue
	4 → 3	59.1	APEX	Pointing Catalogue
U Hya	1 → 0	5.4	SEST	Olofsson et al. (1993)
	2 → 1	17.9	APEX	Pointing Catalogue
	2 → 1	48.8	IRAM	Schöier & Olofsson (2001)
	2 → 1	20.2	JCMT	Schöier & Olofsson (2001)
	2 → 1	13.8	SEST	Schöier & Olofsson (2001)
	3 → 2	25.8	APEX	Pointing Catalogue
	3 → 2	27.2	APEX	Archive
	3 → 2	29.3	APEX	De Beck et al. (2010)
	4 → 3	23.1	APEX	Pointing Catalogue
	4 → 3	30.6	APEX	De Beck et al. (2010)
	7 → 6	25.1	APEX	De Beck et al. (2010)
X TrA	1 → 0	2.5	SEST	Olofsson et al. (1993)
	2 → 1	10.9	APEX	Pointing Catalogue
	2 → 1	11.8	SEST	Olofsson et al. (1993)
	3 → 2	15.0	APEX	Pointing Catalogue
	3 → 2	12.3	APEX	Archive
	3 → 2	15.3	SEST	Schöier & Olofsson (2001)
	4 → 3	19.5	APEX	Pointing Catalogue
II Lup	1 → 0	61	SEST	Ryde et al. (1999)
	2 → 1	118.4	APEX	Pointing Catalogue
	2 → 1	128.12	APEX	Archive
	2 → 1	151	SEST	Ryde et al. (1999)
	3 → 2	163.0	APEX	Ramstedt & Olofsson (2014)
	3 → 2	144.4	APEX	De Beck et al. (2010)
	3 → 2	144.4	APEX	De Beck et al. (2010)
	3 → 2	130.3	APEX	Pointing Catalogue
	3 → 2	122.71	APEX	Archive

Notes. (*) indicates uncorrected ISM contamination.

Table C.1. continued.

Star	Transition	I_{mb} [K km s^{-1}]	Telescope	Reference
	3 → 2	129.3	SEST	Ryde et al. (1999)
	4 → 3	155.9	APEX	De Beck et al. (2010)
	4 → 3	128.4	APEX	De Beck et al. (2010)
	4 → 3	147.0	APEX	Pointing Catalogue
	6 → 5	20.2	HIFI	*Herschel* Science Archive (HIFISTARS)
	7 → 6	151.43	APEX	De Beck et al. (2010)
	7 → 6	82.1	APEX	De Beck et al. (2010)
	10 → 9	19.4	HIFI	*Herschel* Science Archive (HIFISTARS)
	16 → 15	17.2	HIFI	*Herschel* Science Archive (HIFISTARS)
V CrB	1 → 0	11.7	IRAM	Schöier & Olofsson (2001)
	1 → 0	2.7	OSO	Olofsson et al. (1993)
	2 → 1	5.4	APEX	Pointing Catalogue
	2 → 1	18.4	IRAM	Olofsson et al. (1993)
	3 → 2	10.9	APEX	Archive
V821 Her	1 → 0	84.1	IRAM	Neri et al. (1998)
	2 → 1	52.1	APEX	Pointing Catalogue
	2 → 1	93.4	IRAM	Neri et al. (1998)
	3 → 2	60.3	APEX	De Beck et al. (2010)
	3 → 2	56.7	APEX	Pointing Catalogue
	3 → 2	55.9	APEX	Archive
	4 → 3	66.1	APEX	De Beck et al. (2010)
	4 → 3	66.0	APEX	Pointing Catalogue
	4 → 3	81.3	APEX	Archive
	7 → 6	49.8	APEX	De Beck et al. (2010)
V Aql	1 → 0	3.2	OSO	Olofsson et al. (1993)
	1 → 0	2.8	SEST	Olofsson et al. (1993)
	2 → 1	8.8	APEX	Pointing Catalogue
	2 → 1	9.0	JCMT	Schöier & Olofsson (2001)
	2 → 1	8.1	SEST	Olofsson et al. (1993)
	3 → 2	11.5	APEX	Pointing Catalogue
	3 → 2	9	JCMT	Schöier & Olofsson (2001)
V1968 Cyg	1 → 0	46.4	IRAM	Neri et al. (1998)
	2 → 1	88.6	IRAM	Neri et al. (1998)
RV Aqr	1 → 0	7.5	SEST	Olofsson et al. (1993)
	2 → 1	18.1	SEST	Olofsson et al. (1993)
	3 → 2	18.6	SEST	Schöier & Olofsson (2001)
S Stars				
R And	2 → 1	32.0	JCMT	Ramstedt et al. (2009)
	3 → 2	43.0	JCMT	Ramstedt et al. (2009)
	4 → 3	25.6	APEX	Pointing Catalogue
S Cas	1 → 0	13.8	OSO	Ramstedt et al. (2009)
	3 → 2	31.0	JCMT	Ramstedt et al. (2009)
W And	1 → 0	3.8	OSO	Ramstedt et al. (2009)
R Gem	1 → 0	2.4	OSO	Ramstedt et al. (2009)
	2 → 1	4.5	APEX	Pointing Catalogue
	3 → 2	5.2	APEX	Pointing Catalogue
Y Lyn	1 → 0	4.1	OSO	Ramstedt et al. (2009)
R Cyg	1 → 0	4.4	OSO	Ramstedt et al. (2009)
M Stars				
KU And	1 → 0	24.8	OSO	González Delgado et al. (2003)
	2 → 1	14.0	CSO	Knapp et al. (1998)
	2 → 1	41.5	JCMT	González Delgado et al. (2003)
R Hor	2 → 1	19.0	APEX	Pointing Catalogue
	3 → 2	30.8	APEX	Pointing Catalogue
	3 → 2	23	CSO	Young (1995)
	4 → 3	33.5	APEX	Pointing Catalogue
NV Aur	2 → 1	37	JCMT	Kemper et al. (2003)
	2 → 1	36.8	JCMT	González Delgado et al. (2003)
	2 → 1	36.3	JCMT	De Beck et al. (2010)
	3 → 2	39	JCMT	Kemper et al. (2003)
	3 → 2	35.7	JCMT	González Delgado et al. (2003)
	3 → 2	38.8	JCMT	De Beck et al. (2010)
	4 → 3	35.4	JCMT	De Beck et al. (2010)
BX Cam	1 → 0	20.0	OSO	Olofsson et al. (1998)
	2 → 1	25.5	JCMT	Ramstedt & Olofsson (2014)
	3 → 2	39.4	JCMT	Ramstedt & Olofsson (2014)

Table C.1. continued.

Star	Transition	I_{mb} [K km s^{-1}]	Telescope	Reference
GX Mon	1 → 0	31	OSO	Ramstedt et al. (2008)
	2 → 1	56.7	APEX	Pointing Catalogue
	2 → 1	52.9	APEX	Archive
	2 → 1	22.9	CSO	Knapp et al. (1998)
	2 → 1	61	JCMT	Ramstedt et al. (2008)
	3 → 2	64.5	APEX	Pointing Catalogue
	3 → 2	55.0	APEX	Archive
	3 → 2	71	JCMT	Ramstedt et al. (2008)
	4 → 3	54.3	APEX	Pointing Catalogue
	4 → 3	149	JCMT	Ramstedt et al. (2008)
L_2 Pup	1 → 0	0.24	SEST	Kerschbaum et al. (1996)
	2 → 1	3.9	APEX	Pointing Catalogue
	2 → 1	3.1	JCMT	H. Olofsson, (priv. comm.)
	2 → 1	3.7	SEST	Olofsson et al. (2002)
	3 → 2	8.8	APEX	Pointing Catalogue
	3 → 2	16.6	JCMT	Olofsson et al. (2002)
	4 → 3	11.5	APEX	Pointing Catalogue
R LMi	2 → 1	6.1	APEX	Pointing Catalogue
	2 → 1	2.72	CSO	Knapp et al. (1998)
	3 → 2	9.1	APEX	Pointing Catalogue
	3 → 2	12.9	APEX	Archive
R Leo	1 → 0	4.1	IRAM	Teyssier et al. (2006)
	1 → 0	2.1	OSO	González Delgado et al. (2003)
	2 → 1	14.8	APEX	Pointing Catalogue
	2 → 1	28.5	IRAM	Teyssier et al. (2006)
	2 → 1	15.0	JCMT	González Delgado et al. (2003)
	3 → 2	30.3	APEX	Pointing Catalogue
	3 → 2	32.7	APEX	Archive
	3 → 2	21.9	CSO	Knapp et al. (1998)
	3 → 2	41.6	JCMT	González Delgado et al. (2003)
	4 → 3	39.5	APEX	Pointing Catalogue
	4 → 3	28.1	CSO	Young (1995)
	6 → 5	31.0	CSO	Teyssier et al. (2006)
S CrB	2 → 1	6.4	APEX	Pointing Catalogue
	2 → 1	2.53	CSO	Knapp et al. (1998)
	2 → 1	12.7	IRAM	Neri et al. (1998)
	3 → 2	10.6	APEX	Pointing Catalogue
	3 → 2	10.5	APEX	Archive
	3 → 2	9.1	CSO	Young (1995)
	4 → 3	4.9	CSO	Young (1995)
V1111 Oph	1 → 0	21.5	OSO	González Delgado et al. (2003)
	2 → 1	30.6	APEX	Pointing Catalogue
	2 → 1	42.0	JCMT	González Delgado et al. (2003)
	3 → 2	40.5	APEX	Pointing Catalogue
	3 → 2	59.1	JCMT	Ramstedt & Olofsson (2014)
	4 → 3	46.1	APEX	Pointing Catalogue
RR Aql	2 → 1	12.5	APEX	Pointing Catalogue
	2 → 1	16.6	JCMT	H. Olofsson, (priv. comm.)
	3 → 2	16.1	APEX	Pointing Catalogue
	3 → 2	23.5	JCMT	H. Olofsson, (priv. comm.)
	4 → 3	14.3	APEX	Pointing Catalogue
V1943 Sgr	1 → 0	1.25	SEST	Kerschbaum & Olofsson (1999)
	2 → 1	5.17	SEST	Kerschbaum & Olofsson (1999)
V1300 Aql	1 → 0	16	OSO	Ramstedt et al. (2008)
	2 → 1	38.1	APEX	Pointing Catalogue
	2 → 1	45	JCMT	Ramstedt et al. (2008)
	3 → 2	37.0	APEX	De Beck et al. (2010)
	3 → 2	35.3	APEX	Pointing Catalogue
	3 → 2	35.9	APEX	Archive
	3 → 2	27	JCMT	Ramstedt et al. (2008)
	4 → 3	33.5	APEX	De Beck et al. (2010)
	4 → 3	34.8	APEX	Pointing Catalogue
	4 → 3	34.5	APEX	Archive
	4 → 3	22	JCMT	Ramstedt et al. (2008)
	7 → 6	19.7	APEX	De Beck et al. (2010)
T Cep	1 → 0	1.7	OSO	Olofsson et al. (1998)